

2015

Performance Analysis of Separators and Electrolyte and Effects on Solid Electrolyte Interface

Michael L. Lazar
University of Rhode Island, mlazar@snet.net

Follow this and additional works at: https://digitalcommons.uri.edu/oa_diss

Terms of Use

All rights reserved under copyright.

Recommended Citation

Lazar, Michael L., "Performance Analysis of Separators and Electrolyte and Effects on Solid Electrolyte Interface" (2015). *Open Access Dissertations*. Paper 347.
https://digitalcommons.uri.edu/oa_diss/347

This Dissertation is brought to you by the University of Rhode Island. It has been accepted for inclusion in Open Access Dissertations by an authorized administrator of DigitalCommons@URI. For more information, please contact digitalcommons-group@uri.edu. For permission to reuse copyrighted content, contact the author directly.

PERFORMANCE ANALYSIS OF SEPARATORS AND ELECTROLYTE AND EFFECTS
ON SOLID ELECTROLYTE INTERFACE

BY
MICHAEL L LAZAR

A DISSERTATION SUBMITTED IN PARTIAL FULFILMENT OF THE
REQUIREMENT FOR THE DEGREE OF
DOCTOR OF PHILOSOPHY IN CHEMISTRY

UNIVERSITY OF RHODE ISLAND

2015

DOCTOR OF PHILOSOPHY IN CHEMISTRY

OF

Michael L Lazar

APPROVED:

Thesis Committee:

Major Professor	Brett Lucht
	William Euler
	David Heskett
	Nasser H Zawia

DEAN OF THE GRADUATE SCHOOL

UNIVERSITY OF RHODE ISLAND

2015

Abstract

Much of the mobile technology used today (*e.g.* smartphones, tablets, and laptops) is possible because of the lithium ion battery. Because of the high energy density of lithium ion batteries and the continuous improvements in all facets of the technology, larger and more sophisticated batteries are becoming more common for high energy applications such as energy storage for green energy production, electric vehicles (EVs), and hybrid-electric vehicles (HEVs). Despite early success for larger applications, there are some serious problems that still need to be addressed such as cost and battery life. These issues are the motivation for this research.

Utilization of different separators and electrolyte formulations can help achieve sustainable cycling performance and lower cost. The impact on cell performance of electrodes made by a new method to manufacture lithium ion batteries that utilizes ceramic separators is explored, which promises to streamline the manufacture process to lower costs and allow for better performance. Electrodes built using a layer by layer deposition method were cycled and analyzed, including SEM images of the cross section to understand the impact of cycling on the layer interfaces. In addition to knowing how the new manufacturing method can impact the performance of a battery, it is also desired to understand how the separator impacts the performance of the battery. Batteries with ceramic separators are thought to perform better than batteries with polyolefin separators. Cells using ceramic and polyolefin separators were built and cycled extensively at elevated temperature to look for performance differences. In a separate effort to make lithium ion batteries cheaper and perform better, manipulating the electrolyte formulation may be key, especially if ethylene carbonate can be replaced with GBL, and LiPF_6 could be replaced with a more

thermodynamically stable salt such as lithium difluoro(oxalato)borate (LiDFOB). Various LiDFOB electrolyte solutions were made and tested against a standard electrolyte for cycle performance, taken apart, and the surfaces analyzed. The development of a carbonate free electrolyte can be very beneficial to the lithium ion battery, and with thinner and better performing separators, lithium ion battery technology can be better situated for use in large scale applications.

Acknowledgements

I want to thank my advisor, Prof. Brett Lucht for the opportunity to work toward a PhD, Dr. Steve Carlson from Optodot for the funding and supplies for my thesis projects, Dr. Boris Ravdel from Yardney who gave resources used for my thesis projects. I want to thank the many post docs who worked in the Lucht lab while I was here including Dr. Mengqing Xu, Dr. Janak Kafle, Dr. Xiaobo Li, and Dr. Cao Cuong Nguyen who helped me learn about lithium ion batteries and helped solidify my basic chemistry knowledge. I want to also thank colleagues and friends who I worked with at the Lucht group and URI, both past and present.

I would also like to thank my Thesis and Comprehensive Committees which include Dr. Brett Lucht, Dr. William Euler, Dr. David Heskett, Dr. Sze Yang, and Dr. Michael Greenfield.

Preface

This thesis is written in manuscript format. The first chapter is an introduction to lithium ion batteries, Chapter 2 was published in the Journal of Power Sources, and Chapter 3 was published in the Journal of the Electrochemical Society. Chapter 4 will be written in manuscript form, and may be published in the future.

Table of Contents

Abstract.....	ii
Acknowledgements.....	iv
Preface.....	v
Table of Contents.....	vi
Table of Figures and Tables.....	ix
Chapter 1 - Background.....	1
Introduction to Lithium Ion Batteries.....	1
The Basic Components of a Lithium Ion Battery.....	2
How a Lithium Ion Battery Works.....	2
Cathode, Anode, and Separators.....	2
Electrolyte and SEI Formation.....	4
LIB Problems and Solutions Presented in Thesis.....	6
References.....	7
Chapter 2 - Analysis of Integrated Electrode Stacks for Lithium Ion Batteries.....	8
Abstract.....	8
Introduction.....	9
Experimental.....	10
Preparation of the electrodes.....	10
Assembly of the coin cells and Cycling.....	11
Preparation for SEM.....	12
Results.....	12
Cycling of Li/graphite stack and Li/NMC stack cells.....	12
Graphite stack/NMC stack cells.....	13
Elevated Temperature Cycling.....	14
SEM imaging of Electrodes.....	14
Conclusion.....	15
Acknowledgements.....	16
References.....	17
Figures.....	18
Figure 2.1.....	18
Figure 2.2.....	19

Figure 2.3.....	20
Figure 2.4.....	21
Figure 2.5.....	22
Figure 2.6.....	23
Figure 2.7.....	24
Chapter 3 - Carbonate Free Electrolyte for Lithium Ion Batteries Containing γ - Butyrolactone and Methyl Butyrate.....	26
Abstract	26
Introduction	27
Experimental	29
Results and Discussion.....	31
Conductivity	31
Viscosity	32
Electrochemical Cycling.....	32
Electrochemical Impedance Spectroscopy	34
Scanning Electron Microscopy.....	35
X-ray Photoelectron Spectroscopy	36
Infra-Red Spectroscopy	39
Conclusions	40
Acknowledgements	41
References	42
Figures and Tables	44
Figure 3.1.....	44
Figure 3.2.....	45
Figure 3.3.....	46
Figure 3.4.....	47
Figure 3.5.....	48
Figure 3.6.....	49
Figure 3.7.....	50
Figure 3.8.....	51
Figure 3.9.....	52
Figure 3.10.....	53
Table 3.1	54

Table 3.2	55
Table 3.3	56
Chapter 4 - Comparison of Ceramic Containing and Polyolefin Separator Performance in Lithium Ion Batteries	57
Abstract	57
Introduction	57
Experiment	59
Results	61
Cycling.....	61
Electrochemical Impedance Spectroscopy (EIS)	63
XPS Analysis.....	63
FTIR Analysis.....	66
Conclusions	66
Acknowledgements	68
References	68
Figures.....	70
Figure 4.1	70
Figure 4.2.....	71
Figure 4.3.....	72
Figure 4.4.....	73
Figure 4.5.....	74
Figure 4.6.....	75
Figure 4.7.....	76
Figure 4.8.....	77
Table 4.1	78
Table 4.2	79

Table of Figures and Tables

Figure 2.1: Schematic of a graphite/NMC composite cell.....	18
Figure 2.2: Graphite stack / lithium cell discharge capacity at various rates along with cycling efficiency.....	19
Figure 2.3: NMC stack / lithium cell discharge capacity at various rates along with cycling efficiency.....	20
Figure 2.4: Graphite stack / NMC stack cell discharge plot at various rates along with cycling efficiency.....	21
Figure 2.5: Eighth cycle plot of a full cell.	22
Figure 2.6: The efficiency and discharge capacity of a graphite stack / NMC stack cell cycled at 16° C (RT), 55° C, and 16° C (RT), at a C/5 rate.	23
Figure 2.7: Cross sectional SEM images of : A) Fresh graphite stack. B) Fresh NMC stack. C) Cycled graphite stack. D) Cycled NMC stack. E) Graphite stack after cycling at 55° C. F) NMC stack after cycling at 55° C. The graphite stack samples were taken using backscatter electron imaging and the NMC stack samples were taken using secondary electrons imaging. All samples were taken at 20 kV under high vacuum and each image from top to bottom is the current collector, the active material, and the separator.....	25
Figure 3.1: Conductivity measurements of the electrolyte systems used in the cells above.....	44
Figure 3.2: Cycling performance for various electrolyte formulations. The first 55 cycle are at room temperature (RT, 16° C), the next five are at low temperature (LT, -10° C), and the last 20 are at high temperature (HT, 55° C).	45
Figure 3.3: Charge/Discharge plot of the best cells at cycle 30.....	46
Figure 3.4: Electrochemical impedance spectroscopy after 25 cycles, including formation, along with a representative circuit [34]. EC denotes LiDFOB/EC/DMC/DEC electrolyte formulation and GBL denotes LiDFOB/GBL/MB formulation.....	47
Figure 3.5: SEM images for anode of [a]: Fresh [b]: Standard [c]: LiDFOB in EC/DMC/DEC and [d]: LiDFOB in GBL/MB. These samples	

were taken from the best performing samples and are secondary electron images.	48
Figure 3.6: SEM images for cathode of [a]: Fresh [b]: Standard [c]: LiDFOB in EC/DMC/DEC and [d]: LiDFOB in GBL/MB. These samples were taken from the best performing samples and are secondary electron images.	49
Figure 3.7: XPS spectra of the anode extracted from cells cycled with the three different electrolyte formulations. From left to right, the spectra are C 1s, F 1s, O 1s, and B 1s/P2p. From bottom to top is fresh anode, standard electrolyte, LiDFOB in EC/DMC/DEC, and LiDFOB in GBL/MB.	50
Figure 3.8: XPS spectra of the cathodes cycled with the different electrolyte formulations. From left to right, the spectra are C 1s, F 1s, O 1s, and B 1s. From bottom to top is fresh cathode, standard electrolyte, LiDFOB in EC/DMC/DEC, and LiDFOB in GBL/MB.	51
Figure 3.9: FTIR-ATR spectra of anodes.	52
Figure 3.10: FTIR-ATR of cathode samples.	53
Table 3.1: Viscosity of the standard electrolyte and the LiDFOB in GBL/MB electrolyte.	54
Table 3.2: Relative concentration of elements on the surface of the anodes from XPS.	55
Table 3.3: Relative concentration of elements on the surface of the cathodes from XPS.	56
Figure 4.1: 200 [C/5] cycles at HT for the only surviving standard and MTI cells.	70
Figure 4.2: MTI and standard cells cycled at 55° C for 300 cycles at a [C/2] rate. The profile is slightly different than the profile for the same cell types cycled at [C/5].....	71
Figure 4.3: EIS of cells that cycled for 200 HT cycles at a [C/5] rate compared to cells that only cycled formation cycles.	72
Figure 4.4: EIS of cells that cycled for 200 HT cycles at a [C/2] rate compared to cells that only cycled formation cycles.	73
Figure 4.5: XPS of the anode for fresh, standard cells, and MTI cells.	74

Figure 4.6: XPS of the cathode for fresh, standard cells, and MTI cells.....	75
Figure 4.7: FTIR-ATR of anodes for fresh, standard cell and MTI cell.....	76
Figure 4.8: FTIR-ATR of cathode samples fresh, standard cell and MTI cell.	77
Table 4.1: Elemental concentration of anode samples derived from XPS.	78
Table 4.2: Elemental concentration of cathode samples derived from XPS.....	79

Chapter 1 - Background

Introduction to Lithium Ion Batteries

Lithium ion batteries (LIB) are of great interest due to high energy density and high working potentials, making them useful in essential mobile technologies such as smart phones, laptops, and tablets. The reduction potential of lithium vs the standard hydrogen electrode is about -3 V, and lithium is light weight (0.534 g cm^{-3}), giving LIB high energy density [1]. The working potentials of most LIB are in the range of 3.5 to 3.9 V [2], depending on the electrodes used, with the potential working voltages increasing to well over 4 V for newer cathode technologies. The operating potentials for LIB are by far higher than any other secondary battery on the market, where chemistries only allow working potentials of 2 V or fewer [2].

Other than high voltage and great energy density, LIB have other notable advantages. LIB can be designed for high energy purposes or for high power purposes. LIB have a high range of temperature operation from well below freezing to moderately warm temperatures, but the specific range depends on the cell chemistry. While these advantages work in the favor of LIB, they can sometimes work at a disadvantage to LIB. For instance, a battery can be designed for high power or high energy, with one coming at the expense of the other. While LIB can operate at wide temperature ranges, they tend to have lower capacity at lower temperatures. This can be partially mitigated with electrolytes designed to work at low temperatures. At the higher temperature range, LIB work very well, but will lose capacity at an accelerated rate with chronic exposure. Cost is also a disadvantage for larger format batteries as discussed below.

The Basic Components of a Lithium Ion Battery

How a Lithium Ion Battery Works

LIB are composed of a cathode with an aluminum current collector, an anode with a copper current collector, a separator, and electrolyte. The source of lithium is in the cathode material, while the electrolyte facilitates ion movement between the electrodes. Energy is stored at the anode when the intercalated lithium effectively traps electrons. The typical lithium ion battery usually operates between 3.0 to up-to 4.3 V with a working voltage around 3.7 V [2], but new cathode technology can increase the working and cut-off voltages [3].

Cathode, Anode, and Separators

The cathode is made of LMO (lithium metal oxides), where M is cobalt (Co), nickel (Ni), or manganese (Mn), or a combination of these metals. Some commonly used cathode materials are LCO (lithium cobalt oxide), NMC (lithium nickel-manganese-cobalt oxide) and NCA (lithium nickel-cobalt-aluminum oxide, where Al is a minor component).

Other cathodes can be made with metal phosphates, such as LiFePO_4 (lithium iron phosphate) [2, 3]. Capacities of most cathodes is around 150 to 200 mAh g^{-1} , while the working potentials vary from 3.5 to 3.9 V depending on the cell chemistry [2].

Generally, only half of the available lithium in the cathode is used. If too much lithium is taken from the LMO, the structure can collapse causing capacity fade. Work is being done to expand both the specific capacities and the operating potentials [3].

The anode is generally made with graphite. Graphite has a theoretical capacity of 372 mAh g⁻¹, but can vary depending on its form. When lithium is fully intercalated into the anode, six carbons can accommodate one lithium. To expand capacity, there is investigation into silicon, which has a theoretical capacity around 4200 mAh g⁻¹, but has serious issues with volume expansion upon charging [4].

For both the anode and cathode, the active material is combined with binder material, and conducting material if necessary. The active materials are generally granulated, usually at the micron level, and to ensure electrical contact with the current collector, conductive material, such as a conductive carbon are added. Binding material is added to help ensure that the particles stay connected so that capacity can be maintained. Typical binding agents include polyvinylidene difluoride (PVdF), carboxymethylcellulose, or other polymers that are inert in the cell environment [2].

The basic chemical reaction in lithium ion batteries is [2]:



The job of the separator is to allow for ion flow from one electrode to the other while preventing any electron flow, essentially separating the anode from the cathode. The typical separator is made up of polyolefins, usually polypropylene and/or polyethylene, other kinds of polymers, ceramics, and ceramic/polymer blends [5]. Currently,

polyolefins are utilized in most commercial batteries, but ceramic containing separators are gaining lots of attention because they can absorb and retain the electrolyte better and facilitate easy ion transport. The thickness of the separator is on the micron scale, and is typically around 25 μm [5].

Electrolyte and SEI Formation

The main purpose of the electrolyte is to shuttle the lithium ions between the anode and cathode upon charging and discharging the cell. The electrolyte is generally composed of liquid alkyl carbonates, the main ones being ethylene carbonate (EC), diethyl carbonate (DEC), dimethyl carbonate (DMC), and ethyl methyl carbonate (EMC), and a lithium salt, which is lithium hexafluorophosphate (LiPF_6) in most commercial batteries.

Carbonates are used because they can remain stable at the cathode-electrolyte interface for most voltage ranges, and remain stable at the anode-electrolyte interface after the formation of a reductive layer at that interface known as the solid electrolyte interface (SEI) [1, 6-10].

For purposes of SEI formation, EC is paramount. It is readily reduced on the anode during the first charge cycle. While the linear carbonates are more stable on the anode interface than EC is, they also do not bind to the lithium ions as well due to their low dielectric constants. EC on the other hand has a very high dielectric constant, lower, but similar to that of water [1]. However, EC comes with a big downside in that it is a solid at room temperature making the electrolyte viscous as a result. It needs other solvents to make it thinner and to allow it to be conductive enough to work at low temperatures. The linear carbonates as well as various esters have been used to accomplish this [11, 12].

The SEI is a protective layer on the anode/electrolyte interface. This layer forms during the first few cycles to stabilize the electrolyte against the anode surface, which is unstable. Good performing LIB depend on a stable SEI, which will stabilize the electrolyte/electrode interface while allowing ion flow and disallowing electron flow. As mentioned above, EC forms an excellent SEI. Other cyclical carbonates such as propylene carbonate (PC) or vinylene carbonate (VC) have been targeted as SEI forming agents, as are oxalate containing lithium salts such as lithium bis(oxalate)borate and lithium difluoro(oxalate) [1, 6-12].

LiPF₆ is the main salt used in LIB electrolytes because it adequately meets all the major criteria for an electrolyte salt. It dissociates well in solution, dissolves well in carbonate solutions, is stable to all cell parts and can passivate the aluminum current collector, it is thermally stable enough, is relatively safe, and it has very good conductivity [1, 12]. As compared to other possible salts such as LiBF₄, LiAsF₆, LiClO₄, and other salts, it is not the best in every category, but it is good enough in all categories, which cannot be said for its competitors, which often have a fatal flaw in one or more category. Despite being the best candidate, it is not the ideal candidate, and much research has gone into finding a replacement [1, 10]. The major drawbacks of LiPF₆ have to do with thermal stability, and chemical stability in relation to protonated impurities [1, 10, 12-15]. At around 40° C, the LiPF₆ breakdown will accelerate, reacting with protonated solvents that exists in even the cleanest and driest electrolytes, especially water [9, 12-14]. Impurities will react with PF₅, which exists in equilibrium with the LiPF₆ anion, to help create HF and fluorophosphates that can further degrade the electrolyte and react with the SEI or the electrodes to cause degradation and cell failure [10, 13, 14].

LIB Problems and Solutions Presented in Thesis

While lithium ion batteries have many advantages, it is the disadvantages that hold it back for larger scale uses. In order to be viable for the automobile market, LIB have to last more than 15 years, must be safe, and sell at lower costs [16]. Many of the Department of Energy goals for LIB include lowering costs to \$125 per kWh [16] of useable energy from somewhere near \$300 per kWh today [16], achieve energy densities of 400 Wh L⁻¹ and 250 Wh kg⁻¹ [16], and achieve a power density of 2000 W kg⁻¹ by 2022 [16].

The research presented in this thesis is intended to help improve LIB with the DOE goals in mind. Working with Optodot as a collaborator, studies looking into electrodes made with alternative manufacturing processes, studying alternative electrolyte solutions, and studying the separator effects on cell performance can be a key to reaching DOE goals. With alternative manufacturing, the goal is to increase energy density by reducing the amount of non-active materials used in the cell such as the separator and current collectors while providing a cell that can perform as well or better than conventionally built cells. The alternative manufacturing can also help to lower the costs of the manufacturing process. In formulating alternative electrolytes, it is possible to reduce the cost of the electrolyte while eliminating problematic solvents such as EC. Lastly, understanding how well different separators work in a cell can be a key to identifying the best separator formulations to use in future LIB. The separator can aid or hinder cell longevity, and understanding why can help make batteries last longer.

References

- [1] K. Xu, *Chem. Rev.*, **104**, 4303 (2004).
- [2] J. Dahn, G.M. Ehrlich, Lindon's Handbook of Batteries, 4th Edition, T.B. Reddy, Ch. 26, McGraw Hill, New York, (2011).
- [3] M.S. Whittingham, *Chem.Rev.*, **114**, 11414 (2014).
- [4] C.K. Chan, H. Peng, G. Liu, K. McIlwrath, X.F. Zhang, R.A. Huggins, Y. Cui, *Nature Nanotech.*, **3**, 31 (2007).
- [5] S.S. Zhang, *J. Power Sources*, **164**, 351 (2007).
- [6] P. Verma, P. Maire, and P. Novák, *Electrochim. Acta*, **55**, 6332 (2010).
- [7] M. Nie and B.L. Lucht, *J. Electrochem. Soc.*, **161**, A1001 (2014).
- [8] K. Xu, *Energies*, **3**, 135 (2010).
- [9] M. Nie, D. Chalasani, D.P. Abraham, Y. Chen, A. Bose, and B.L. Lucht, *J. Phys. Chem. C*, **117**, 1257 (2013).
- [10] K. Xu, *Chem. Rev.*, **114**, 11503 (2014).
- [11] M.C. Smart, B.V. Ratnakumar, K.B. Chin, and L.D. Whitcanack, *J. Electrochem. Soc.*, **12**, A1361 (2010).
- [12] V. Aravindan, J. Gnanaraj, S. Madhavi, and H-K Liu, *Chem. Eur. J.*, **17**, 14326 (2011).
- [13] C.L. Campion, W. Li, and B.L. Lucht, *J. Electrochem. Soc.*, **152**, A2327 (2005).
- [14] S. E. Sloop, J. B. Kerr, and K. Kinoshita, *J. Power Sources*, **119-121**, 330 (2003).
- [15] W. Li, C. Campion, B. L. Lucht, B. Ravdel, and K. M. Abraham, *J. Electrochem. Soc.*, **152**, A1361 (2005).
- [16] Vehicle Technologies Office: 2013 Energy Storage R&D Progress Report, Department of Energy. <http://energy.gov/eere/vehicles/downloads/vehicle-technologies-office-2013-energy-storage-rd-progress-report-sections> (Accessed 01 Oct. 2014).

Chapter 2 - Analysis of Integrated Electrode Stacks for Lithium Ion Batteries

Michael Lazar^a, Ben Sloan^b, Steven Carlson^b, Brett Lucht^a

^aUniversity of Rhode Island, Kingston, RI 02881

^bOptodot Corporation, 2 Kingsbury Ave, Watertown, MA

Journal of Power Sources, Vol. 251, p.476, 2014.

Abstract

In an effort to reduce the cost of manufacturing lithium ion batteries, a novel approach is being developed to build a one piece integrated cell via layer by layer coating deposition rather than manufacturing separate pieces followed by electrode stacking and assembly. This new process would hold several advantages by providing excellent contact and thinner deposits, which will conserve space for energy storing materials while reducing production costs. Anode and cathode half stacks are made using a new process and the electrodes have been investigated in coin cells. Each half stack consists of a current collector, electrode, and separator combined into a single component. The stack cells successfully cycle as graphite stack / lithium and $\text{LiNi}_{1/3}\text{Mn}_{1/3}\text{Co}_{1/3}\text{O}_2$ / lithium cells and together in graphite stack / $\text{LiNi}_{1/3}\text{Mn}_{1/3}\text{Co}_{1/3}\text{O}_2$ stack cell arrangements. Cross sectional SEM images show very little change in the anode and cathode materials indicating that the material is stable under typical cycling conditions and at moderately elevated temperature (55 °C). While

the electrode stacks investigated are not optimized, the results support good cycling performance for a stacked cell design.

Introduction

Improvement of the cell design of lithium ion batteries is important to lowering manufacturing costs, which is one of the major hurdles for the widespread implementation of lithium ion batteries into electric vehicles [1]. A novel approach to lowering the manufacturing cost of lithium ion batteries is to build cells via a layer by layer coating deposition process as opposed to the current preparation via slurry coated electrodes and free-standing separators which are then assembled via stacking or winding. The layer by layer method can further benefit cells by providing thinner layers, which have the potential to conserve space, improve the volumetric energy density, and decrease the quantity of inactive components (separator, current collectors, and electrolyte) and thus the cost of the materials within the cell. This process also has the potential for battery preparation via layering electrodes in a single manufacturing process, allowing most of the work to be accomplished through automation reducing the coating and assembly cost. The concept of a cell stack has been investigated but there are few reports in the literature [2-5]. Most of the research in this area has focused on the development of novel separators rather than developing an electrode stack [6]. These investigations focused on polymer separators with ceramic additives [2-4,7,8], or developing separators consisting of ceramic and binder [5]. Since the idea of a stacked cell has not been significantly studied or optimized, the goal of this research was to develop a method to prepare a cell stack with comparable performance to traditional cells.

Experimental

Preparation of the electrodes

Anode stacks are composed of approximately 13 μm of separator, 43 μm of graphite anode and 11 μm of copper. The cathode stacks are composed of approximately 10 μm of separator, 73 μm of $\text{LiNi}_{1/3}\text{Mn}_{1/3}\text{Co}_{1/3}\text{O}_2$ (NMC) cathode and 11 μm of aluminum. Each stack is layered into one bonded and inseparable piece rather than existing as separate pieces of metal/electrode and separator as in the current manufacturing process for cells. The graphite anodes and NMC cathodes (92% active material along with PVdF binder and conductive carbon) were coated directly onto the ceramic separator layer. This is afforded by the small pores of the ceramic separator (30 nm diameter) which prevent penetration of the electrode materials into the separator layer.

The anode stacks were made by first coating a separator layer of aluminum boehmite and polymer onto a silicone-treated polyester release film. The porosity of the separator layer was approximately 43%. The average pore size diameter of the separator layer was approximately 30 nm with a very narrow pore size distribution. Next, a commercial graphite anode layer was coated onto the separator layer. Then, the copper layer was sputtered onto the anode layer, followed by delamination of the release substrate to provide the anode stack. The cathode stacks were made similarly by coating a commercial NMC cathode onto the separator layer on the release film and then sputtering an aluminum layer onto the cathode layer. Delaminating the release film provided the cathode stack.

Assembly of the coin cells and Cycling

Each sample was evaluated in a coin cell versus lithium metal. The electrode stacks were cut to a diameter of 14.7 mm and assembled in a coin cell using 40 μL of electrolyte (1M LiPF_6 in 1:1:1 ethylene carbonate/dimethyl carbonate/diethyl carbonate (EC/DMC/DEC) [9]) and a protective polyolefin separator ring with an inner diameter of 12 mm and an outer diameter of 19 mm. The separator, which is about 10 μm thick, is only large enough to cover the electrode. A polyolefin ring was used to prevent possible shorting at the edges of the electrode due to the presence of loose particles resulting from electrode cutting and may contact the lithium electrode and result in shorting.

Both the Li/graphite and Li/NMC cells were initially cycled at a C/20 rate for five cycles followed by five C/10 cycles, ten C/5 cycles, ten C/2 cycles, and three C/20 cycles. The total capacity of each Li/graphite composite cell was about 3.4 mAh and the total capacity of each Li/NMC composite cell was about 4.2 mAh. Additionally, graphite/NMC cells were prepared with a 15 mm diameter graphite/separator stack and a 12.7 mm diameter NMC/separator stack. The theoretical capacity of the cell is 3.1 mAh and is cathode limited. The cells were cycled with the same profile as discussed above. The full cells also contain the protective polyolefin ring used in the half cells to prevent shorting from the edges of the electrodes. Figure 2.1 depicts the configuration of the graphite stack/NMC stack cell.

Additionally, full cells were prepared and cycled at 55° C to simulate accelerated aging. The cells were full cells constructed as above and used 30 μL of electrolyte. The formation cycling was one cycle at C/20 followed by two cycles at C/10 and two cycles at C/5 rates.

The cells were then cycled at a C/5 rate for ten cycles at 16° C, ten cycles at 55° C and ten cycles at 16° C.

Preparation for SEM

The electrode stacks were imaged using cross sectional SEM with fresh electrode stacks and electrode stacks cycled in graphite/NMC cells. The fresh samples were prepared by cutting a piece of a small part of the electrode with a razor blade with the separator side facing the blade. Cycled cells were opened in an argon filled glove box, rinsed three times with dimethyl carbonate, and vacuum dried overnight to remove the excess DMC then cut with a razor blade.

Results

Cycling of Li/graphite stack and Li/NMC stack cells

The cycling efficiencies of the Li/graphite stack cells during the initial formation cycles are lower (40 - 80 %) than is typically observed for Li/graphite cells (70-80 %). However, after the formation cycles (first five cycles) the cycling efficiency is very good, > 99 % (Figure 2.2). Much better first cycle efficiency (~85 %) is observed for graphite stack/NMC stack cells, as discussed below. Thus, the low efficiency during formation cycling may result from detrimental interactions between the lithium metal and the edges of the cut electrode stack. The capacity drops significantly for Li/graphite cells with increased cycling rates. Only ~30 mAh g⁻¹ (~10 % of the initial capacity) is obtained from cells cycled at C/2. However, the capacity lost upon cycling at high rate can be recovered

with low rate cycling consistent with slow kinetics as opposed to irreversible capacity loss. Despite the poor rate performance, the efficiency of the Li/graphite cells is very good at all rates ($> 99\%$). The Li/NMC stack cells have good first cycle efficiency (85 - 90%) and discharge capacity (145 mAh g^{-1}). Upon cycling at higher rates the Li/NMC stack cells retain good efficiency ($> 95\%$) and discharge capacity at C/10 and C/5, but the capacity drops off at higher rate (C/2, Figure 2.3). In general, both the Li/graphite stack and Li/NMC stack cells have satisfactory performance. Thus, graphite stack/NMC stack cells were prepared and investigated.

Graphite stack/NMC stack cells

Graphite stack/NMC stack cells were prepared and cycled (Figure 2.4). The first cycle efficiency is 85 % and the discharge capacity is 150 mAh g^{-1} . The irreversible capacity on the first cycle is consistent with the formation of a solid electrolyte interface (SEI) on the graphitic anode [10]. The cells retain high capacity as the cycling rate is increased from C/20 to C/2. The cells still deliver 120 mAh g^{-1} at the fastest rate (C/2) and the cycling efficiency is high for all cells, $>98\%$. After cycling at high rate, the cells are able to deliver $> 90\%$ of the initial capacity at C/20 (140 mAh g^{-1}) suggesting that the cells have stable cycling performance. The cycling performance is comparable to standard graphite/NMC cells prepared with traditional polyolefin separators [11].

The charge-discharge plot of the eighth cycle is provided in Figure 2.5. The charge and discharge plots are symmetrical with a small hysteresis, and are typical for graphite/NMC cells further supporting comparable performance of the graphite/separator stack and NMC/separator stack electrodes to traditional coated electrodes with polyolefin separators.

Elevated Temperature Cycling

Additional graphite stack/NMC stack cells were cycled at 55° C to simulate accelerated aging and is depicted in Figure 2.6. The cells cycled well, with only an 8 % capacity loss during the ten cycles at 55° C. Upon returning the cells to 16° C after cycling at 55° C, the cells retained 88 % of the initial RT capacity. The good cycling stability at elevated temperature can be attributed to the good thermal stability of the separator and the Lewis basic nature of the aluminum boehmite [12]. The cycling performance of the first generation electrode separator stacks suggests that separated coated electrode stacks may be a viable option for the next generation of lithium ion batteries. To better understand the structure of the electrode stacks before and after cycling at 16° C and 55° C, cross sectional SEM images of the electrodes were obtained.

SEM imaging of Electrodes

SEM cross sectional images of the graphite separator stack and the cathode separator stack, both fresh and after cycling, are provided in Figure 2.7. For the anode images, the copper is the bright material at the top of the image and is approximately 11 μm thick. The dark material in the center of the image is the active graphite anode material and has a thickness of 40-45 μm and the separator is the smooth, light colored material at the bottom of the image with a thickness around 13 μm. The top of the anode stack has a significant undulation due to variations in the thickness of the active graphite layer which is likely due to a lack of calendaring of the samples. After cycling the top surface is somewhat smoother, presumably due to the stack pressure within the cell. Otherwise, there are no

significant changes to the electrode materials suggesting that the graphite stack anode is stable upon cycling.

The cathode stack is more uniform than the anode stack. The top bright layer is the sputtered aluminum. The aluminum layer is approximately 11 μm thick but it is difficult to distinguish due to the similarity of brightness to the cathode material. However, the aluminum aggregates are smoother and smaller particles than the active metal oxide. The active NMC layer is in the center and is 70-75 μm thick and the separator is smooth layer at the bottom of the image and is about 10 μm thick. The separator has some bright spots due to charge build up during imaging. The cross section SEM images for the cycled cathode stacks do not differ significantly from the images of the fresh cathode stacks which indicate that the cathode is stable to cycling.

SEM images of the electrodes after cycling at 55° C are provided in Figure 2.7, images E and F. The images are similar to the images of the fresh electrodes and electrodes extracted from cells cycled at 16° C. There is no evidence of damage to either the graphite stack electrode or the NMC stack electrode.

Conclusion

Layered electrode stacks were prepared with copper/graphite/separator and aluminum/NMC/separator. The layered electrode stacks were cycled with lithium metal anodes. The Li/ graphite stack cells have poor first cycle efficiency, but have high discharge capacity after the first cycle $\sim 250 \text{ mAh g}^{-1}$. The Li/ NMC stack cells have good

first cycle efficiency and reasonable discharge capacity (145 mAh g⁻¹) and good rate performance up to C/5. However, the graphite stack/NMC stack cells have the best performance. The cells have high first cycle reversibility (85 %), good capacity (150 mAh g⁻¹) and good rate performance up to C/2. These cells also cycle well at 55° C consistent with good calendar life performance. Ex-situ analysis of the electrode stacks before and after cycling suggest that cycling does not induce significant changes to the electrode stack structure and is consistent with good cycling behavior, even at 55° C. The results suggest that the use of layered stack electrodes is a promising alternative for the preparation of lithium ion batteries.

Acknowledgements

Special thanks for the funding of this project go to Optodot and the U.S. Department of Energy grant number DE-EE0005433.

References

- [1] J. B. Goodenough, *Acc. Chem., Res.* **46**, 1053 (2013).
- [2] J. M. Tarascon, A. S. Gozdz, C. Schmutz, F. Shokoohi, P. C. Warren, *Solid State Ionics*, **86-88**, 49 (1996).
- [3] R. A. M. Hikmet, *J. Power Sources*, **92**, 212 (2001).
- [4] P. P. Prosini, P. Villano, M. Carewska, *Electrochimica Acta*, **48**, 227 (2002).
- [5] J. Chen, H. Xiang, Zhang, L. H. Wang, *J. Appl. Electrochem.*, **42**, 471 (2012).
- [6] S. S. Zhang, *J. Power Sources*, **164**, 351 (2007).
- [7] A. Du Pasquier, P. C. Warren, D. Culver, A. S. Gozdz, G. G. Amatucci, J. M. Tarascon, *Solid State Ionics*, **135**, 249 (2000).
- [8] W-K Shin, D-W Kim, *J. of Power Sources*, **226**, 54 (2013).
- [9] M. C. Smart, B. V. Ratnakumar, S. J. Surampudi, *Electrochem. Soc.*, **146**, 486 (1999).
- [10] M. Nie, D. Chalasani, D. P. Abraham, Y. Chen, A. Bose, B. L. Lucht, *The Journal of Physical Chemistry C*, **117**, 1257 (2013).
- [11] I. Bloom, L.K. Walker, J.K. Basco, D.P. Abraham, J.P. Christopherson, C.D. Ho, *J. of Power Sources*, **195**, 877 (2010).
- [12] W. Li, C. Champion, B. L. Lucht, B. Ravdel, and K. M. Abraham, *J. Electrochem Soc.*, **152**, A1361 (2005).

Figures

Figure 2.1

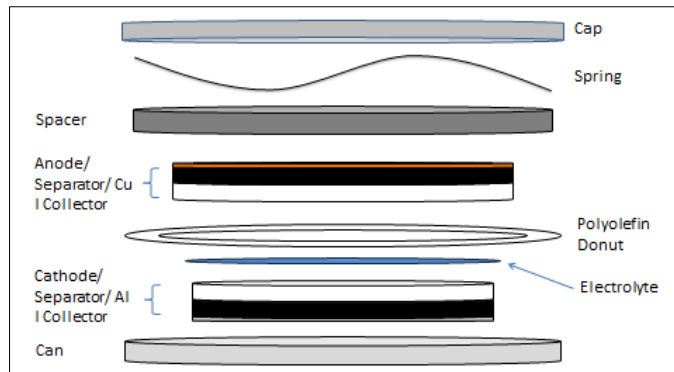


Figure 2.1: Schematic of a graphite/NMC composite cell.

Figure 2.2

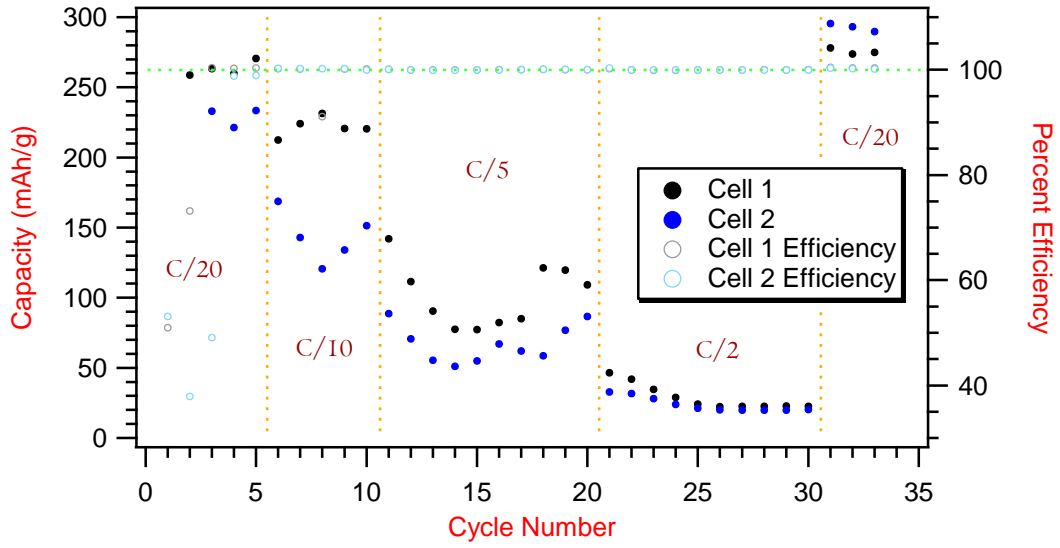


Figure 2.2: Graphite stack / lithium cell discharge capacity at various rates along with cycling efficiency.

Figure 2.3

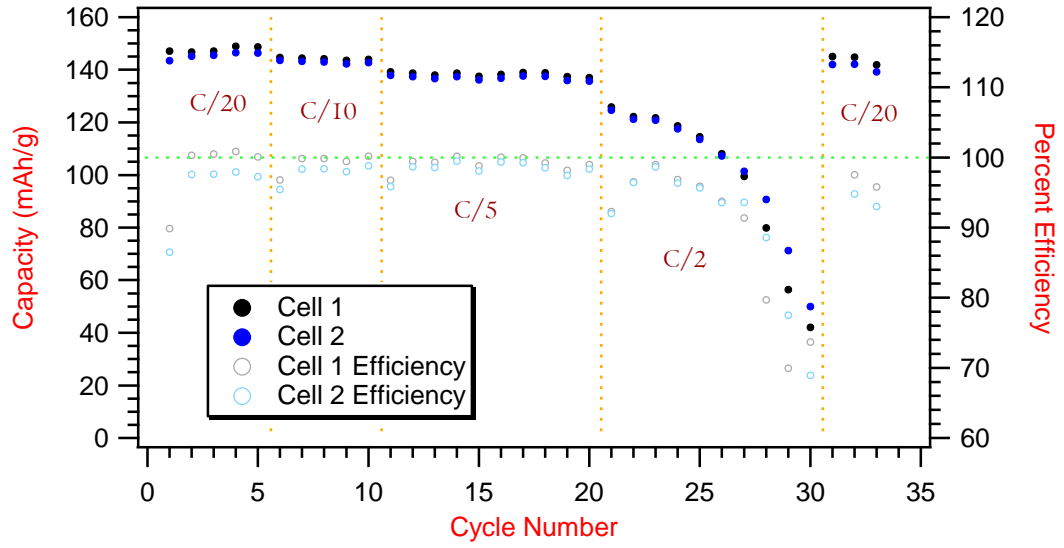


Figure 2.3: NMC stack / lithium cell discharge capacity at various rates along with cycling efficiency.

Figure 2.4

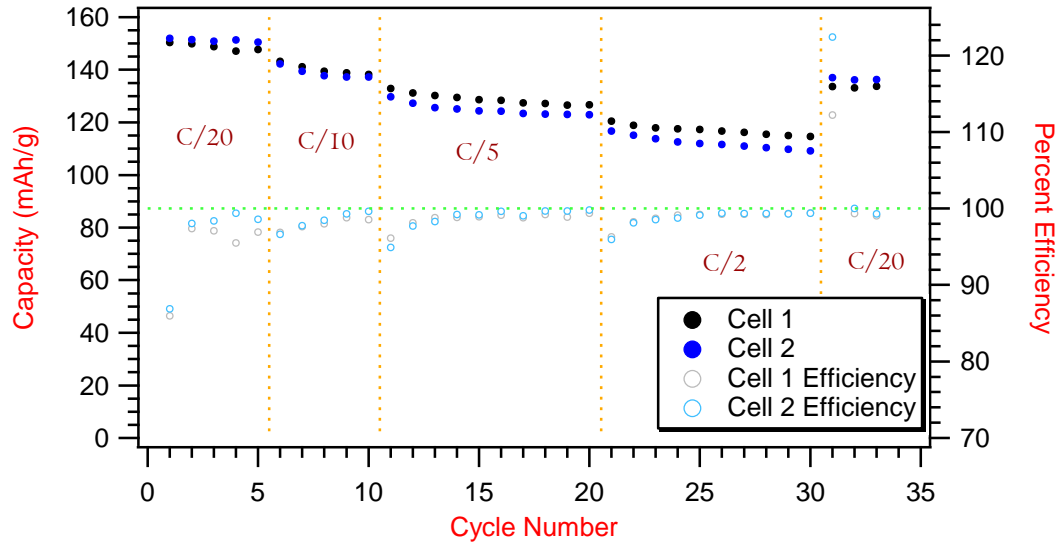


Figure 2.4: Graphite stack / NMC stack cell discharge plot at various rates along with cycling efficiency.

Figure 2.5

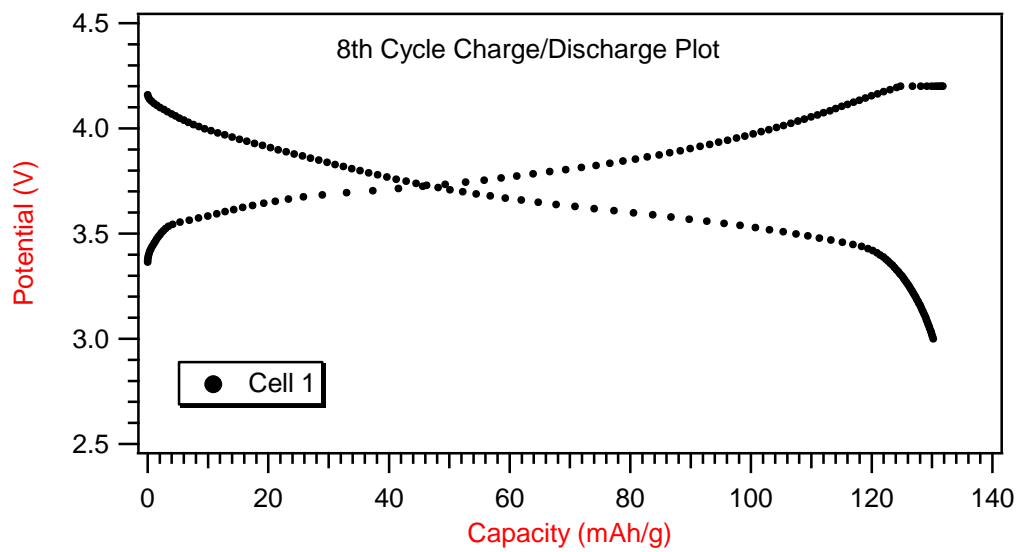


Figure 2.5: Eighth cycle plot of a full cell.

Figure 2.6

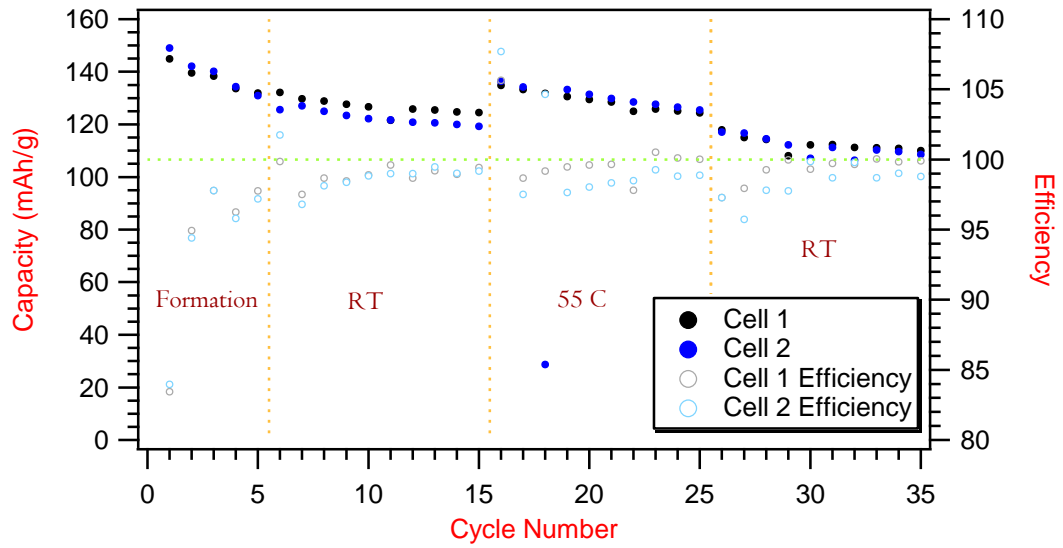


Figure 2.6: The efficiency and discharge capacity of a graphite stack / NMC stack cell cycled at 16° C (RT), 55° C, and 16° C (RT), at a C/5 rate.

Figure 2.7

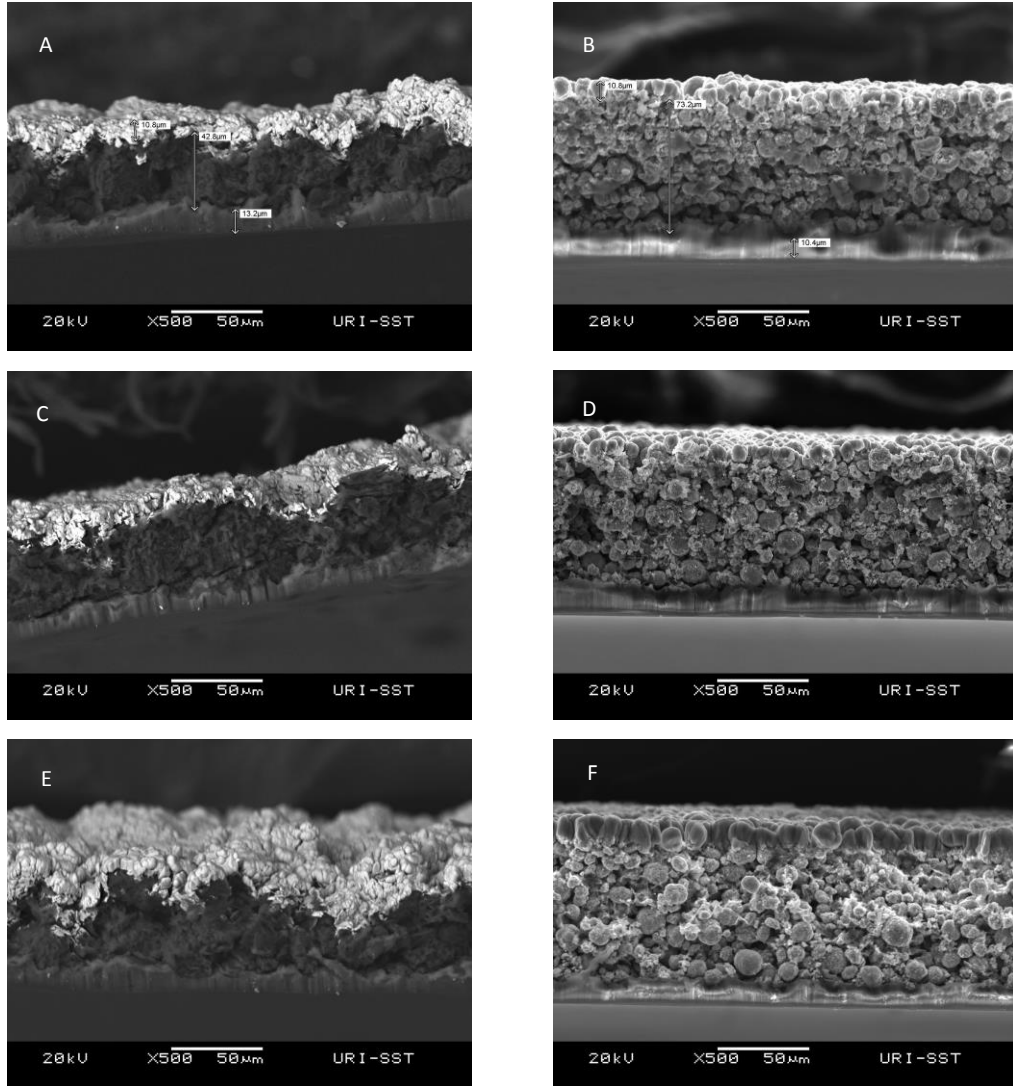


Figure 2.7: Cross sectional SEM images of : A) Fresh graphite stack. B) Fresh NMC stack. C) Cycled graphite stack. D) Cycled NMC stack. E) Graphite stack after cycling at 55° C. F) NMC stack after cycling at 55° C. The graphite stack samples were taken using backscatter electron imaging and the NMC stack samples were taken using secondary electrons imaging. All samples were taken at 20 kV under high vacuum and each image from top to bottom is the current collector, the active material, and the separator.

Chapter 3 - Carbonate Free Electrolyte for Lithium Ion Batteries Containing γ -Butyrolactone and Methyl Butyrate

Michael L. Lazar, Brett L. Lucht

Department of Chemistry, University of Rhode Island, Kingston, RI 02881, USA

Journal of the Electrochemical Society, Vol. 162, A928, 2015.

Abstract

A novel carbonate free electrolyte, 1 M lithium difluoro(oxalate) borate (LiDFOB) in 1:1 *gamma*-butyrolactone (GBL)/methyl butyrate (MB), has been compared to a standard electrolyte, 1 M LiPF₆ in 1:1:1 EC/DMC/DEC, and a 1 M LiDFOB in 1:1:1 EC/DMC/DEC electrolyte. The conductivity of 1 M LiDFOB in GBL/MB is higher at low temperature, but slightly lower at higher temperature compared to the standard electrolyte. The 1 M LiDFOB in GBL/MB electrolyte has comparable cycling performance to the standard electrolyte, and better cycling performance than the 1 M LiDFOB in EC/DMC/DEC electrolyte. The reversible cycling performance suggests that the LiDFOB in GBL/MB electrolyte forms a stable anode solid electrolyte interface (SEI) in the presence of GBL. Ex-situ surface analysis of the extracted electrodes has been conducted via a combination of XPS, FTIR-ATR and SEM which suggests that the stable anode SEI results is primarily composed of reduction products of LiDFOB.

Introduction

The widespread implementation of electric vehicles (EVs) requires further improvements in lithium ion batteries [1, 2, 3]. Some of the biggest challenges for lithium ion batteries in EVs are cost, low temperature performance and battery lifetime [2, 3]. Improvements in the electrolyte can assist in the resolution of each of these problems [1, 4, 5]. Most commercial electrolytes are composed of LiPF_6 in a mixture of carbonate solvents [5]. However, the high cost and poor thermal and hydrolytic stability of LiPF_6 is problematic for the electrolyte [6, 7, 8]. In addition, ethylene carbonate (EC) is typically a required component of the electrolyte due to the role of EC in the formation of the solid electrolyte interphase (SEI) on the anode [5, 9-14]. Since EC is a solid at room temperature, electrolytes containing EC frequently have poor performance at low temperature [15]. Despite the shortcomings of LiPF_6 / EC based electrolytes, these formulations have proven very difficult to replace. While there have been significant efforts to develop novel electrolytes with superior performance to LiPF_6 in carbonates, there has been limited success. The development of novel solvent systems has been more limited and frequently targeted toward specific problems such as high voltage cathodes, salt solubility, or reactivity issues [16-21]. The development of novel salts has encountered problems related to salt solubility and corrosion of the aluminum current collector on the cathode [21, 22].

One of the more interesting and promising alternative salts is lithium difluoro(oxalato) borate (LiDFOB) [1, 4, 23, 24]. LiDFOB is promising due to good solubility, thermal stability, passivation of the aluminum current collector, stable SEI formation, and potentially lower cost. While there have been a limited number of investigations of

LiDFOB as the conducting salt in the electrolyte [4, 16, 25], there have been several reports of the use of LiDFOB and the related salts lithium bis(oxalato) borate (LiBOB) and lithium tetrafluoro(oxalato) phosphate (LiTFOP) as additives to LiPF_6 based electrolytes to form a more stable SEI [1, 14, 23, 26-30]. There have also been reports of the use of oxalate salts enabling the cycling of PC based electrolytes due to better SEI formation [30]. The presence of the oxalate group in the anode thus may enable the use of EC free electrolytes and electrolytes with non-carbonate solvents.

The investigation of LiDFOB has been expanded to include carbonate free electrolyte formulations. Esters and lactones are an interesting alternative to carbonate solvents. Linear esters have been studied as co-solvents due to the high dielectric constants and low freezing points which have been reported to improve the low temperature performance of lithium ion batteries, [15] while lactones such as γ -butyrolactone (GBL) have high dielectric constants [5] and a very wide liquid temperature range (-43.5 to 204 °C). However, the use of GBL as a primary solvent in lithium ion battery electrolytes has been plagued by problems with the stability of the anode SEI [5]. Despite the issues with GBL as a solvent in carbonate based electrolytes, GBL has been studied with LiBOB based electrolytes due to the limited solubility of LiBOB in carbonates [18, 31]. In order to investigate the use of novel electrolyte formulations for lithium ion batteries, a comparative study of three electrolytes has been conducted; a standard LiPF_6 electrolyte in 1:1:1 EC/ dimethyl carbonate (DMC)/ diethyl carbonate (DEC) was tested against 1 M LiDFOB in 1:1:1 EC/DMC/DEC and 1 M LiDFOB in 1:1 GBL/MB (MB is methyl butyrate).

Experimental

LiDFOB was made following previously published procedures [4]. The standard electrolyte 1 M LiPF₆ in 1:1:1 EC/DMC/DEC, and battery grade solvents EC, DMC, and DEC were provided by BASF. GBL and MB were purchased from Sigma Aldrich in high purity and were dried with molecular sieves. The GBL was also distilled. 1 M LiDFOB in EC/DMC/DEC (1:1:1 by volume) and 1 M LiDFOB in GBL/MB (1:1 by volume, as a simple binary solvent system) were prepared in an argon filled glove box. 2032 coin cells were prepared with an anode composed of G5 graphite (89% G5 Graphite, 2% Super P carbon, 8.9% PVdF, 0.1% adhesive enhancer) and a cathode composed of LiNi_{0.80}Co_{0.15}Al_{0.05}O₂ (89% LNMAO, 2% KS15 graphite, 2% SAB, 2% Super P carbon, 5% PVdF) and were provided by Yardney Technical Products. The separator was polyolefin (polyethylene) Setela E20MMS.

Conductivity measurements were acquired between -20° C and 40° C with an Orion 3 Star conductivity meter from Thermo Scientific. 10 to 15 mL of electrolyte was added to a glass tube and sealed. The samples were allowed to equilibrate at each temperature for at least two and a half hours. The experiment was carried out in a Tenney JTR environmental chamber.

Viscosity measurements were taken using a glass capillary viscometer. Using the well-established density and viscosity of water at 20° C [32], the viscosities of the standard 1M LiPF₆ in EC/DMC/DEC and the 1M LiDFOB in GBL/MB were calculated using Equation 1:

$$\eta_2 = \frac{\eta_1 \times \rho_2 t_2}{\rho_1 t_1}$$

Equation 1

Where η , ρ , and t are viscosity in mPa s, density in g mL^{-1} , and time in seconds. The average time and standard deviation were also calculated. The samples were maintained in an environmental chamber set at 20°C for at least four hours to ensure that the temperature was constant. Density was calculated for the samples in a 10 mL volumetric flask and with the sample at 20°C .

To test the cycling performance of the electrolyte formulations, three replicate cells of each electrolyte formulation underwent formation cycling that consisted of one C/20 cycle, followed by two C/10 cycles, and concluded with two C/5 cycles at 16°C . Each set of cells was then cycled for 50 additional cycles at a C/5 rate. The C rates were based on theoretical capacity. After cycling the cells at room temperature, cells were cycled at a rate of C/5 for five cycles with the charge at 25°C and discharged at -10°C , to investigate the low temperature discharge performance, and cells were cycled for 20 C/5 cycles at 55°C , to study accelerated aging.

Electrochemical impedance spectroscopy (EIS) was conducted on cells after 25 cycles at 16°C . Cells were charged at a C/5 rate to 4.1 V followed by holding at constant voltage for 10 hours. For EIS measurements, the cells were held again at constant voltage of 4.1V for a half hour, and EIS was taken from 300 kHz to 20 mHz.

Cells were opened in an argon filled glove box and washed three times with anhydrous DMC to remove the electrolyte and then dried overnight at room temperature under vacuum for surface analysis. FTIR-ATR (Fourier Transform Infrared Spectroscopy – Attenuated Total Reflectance) was acquired with a Bruker TENSOR 27 spectrometer

with a germanium crystal and ATR accessory, and was purged continuously with nitrogen. Samples were analyzed at two separate locations on the electrode from 800 to 4,000 cm^{-1} with 128 scans. The SEM (Scanning Electron Microscope) images were taken using a JEOL 5900 at high vacuum and are secondary electron images. The samples briefly exposed to air during transfer from the glove box to the SEM. The XPS (X-ray Photoelectron Spectroscopy) was conducted with a PHI 5500 system using Al $K\alpha$ radiation source ($h\nu = 1486 \text{ eV}$) under ultrahigh vacuum. The spectra were analyzed and fitted by Multipak 6.1 and XPS peak software (version 4.1). Line syntheses of elemental spectra were conducted using Gaussian–Lorentzian (80:20) curve fitting. The concentrations (C_x) of each element were calculated based on Equation 2:

$$C_x = \frac{(I_x/S_x)}{\sum(I_i/S_i)}$$

Equation 2

where I_x is the intensity of the relative element, and S_x is the sensitivity number of the element, the values obtained from the Multipak software [29]. The C1s graphite (C-C) peak at 284.3 eV was used to confirm the binding energy scale and the F1s peak for LiF at 685.0 eV was used as a secondary reference [14, 21, 33].

Results and Discussion

Conductivity

The conductivities of the three electrolytes are depicted in Figure 3.1. The conductivity of the standard electrolyte, 1 M LiPF_6 in 1:1:1 EC/DMC/DEC, and the conductivity of

the LiDFOB/GBL/MB electrolyte, 1 M LiDFOB in 1:1 GBL/MB, are similar at room temperature. The standard electrolyte is slightly better than the LiDFOB in GBL/MB electrolyte at elevated temperatures, while the LiDFOB in GBL/MB electrolyte has better conductivity at lower temperatures. This suggests that the LiDFOB in GBL/MB electrolyte may afford better performance at low temperature. In contrast, the 1 M LiDFOB in 1:1:1 EC/DMC/DEC electrolyte has lower conductivity than the standard electrolyte or the LiDFOB in GBL/MB electrolyte. Interestingly, the conductivity of the two LiDFOB electrolytes have a parallel relationship.

Viscosity

The viscosity of the standard electrolyte is slightly higher than the viscosity of LiDFOB in GBL/MB electrolyte as provided in Table 3.1, with the standard electrolyte having a viscosity of 3.57 mPa s and the LiDFOB in GBL/MB electrolyte having a viscosity of 2.94 mPa s. The lower viscosity of the LiDFOB in GBL/MB electrolyte can be attributed to the lower density of the electrolyte and the low viscosities of the solvents. The higher viscosity of the standard electrolyte is partially due to the higher density, but largely due to the high viscosity of EC.

Electrochemical Cycling

The cells containing 1 M LiDFOB electrolytes cycle comparably to the cells containing standard electrolyte (Figure 3.2). The cells containing standard electrolyte have an initial capacity of $\sim 120 \text{ mAh g}^{-1}$ after formation cycling, but the capacity slowly rises during

the next 25 cycles to reach a maximum of 150 mAh g⁻¹. This may be due to slow wetting of the electrode with the EC based electrolyte. The 1 M LiDFOB in EC/DMC/DEC electrolyte has similar capacity to the cell containing the standard electrolyte except that the maximum capacity is slightly lower, 140 mAh g⁻¹. The LiDFOB in GBL/MB electrolyte does not follow the same gradually increasing capacity profile of the EC based electrolytes. A constant capacity between 140 and 150 mAh g⁻¹, is maintained from the end of formation cycling throughout the next 50 cycles with a slight fade in capacity. The first cycle efficiency of the cells with the standard electrolyte is 68%, while the cells containing LiDFOB in EC/DMC/DEC and LiDFOB in GBL/MB have comparable first cycle efficiencies of 67 and 72 %, respectively. The efficiencies stabilize around 99% for cells containing all electrolytes investigated.

In order to understand the performance of the novel electrolytes at different temperature extremes as required for EV applications, low temperature (-10 °C) discharge performance and moderately elevated temperature (55 °C) accelerated aging cycling performance were investigated. Cells containing standard electrolyte have the best discharge capacity (~135 mAh/g) during low temperature discharge (-10° C), while cells containing the LiDFOB in GBL/MB electrolyte have slightly lower discharge capacity (~115 mAh/g) and cells containing the LiDFOB in EC/DMC/DEC have the worst discharge performance (~20 mAh/g). Upon cycling cells at 55° C, a slight increase in capacity, compared to the RT cycling capacities, is observed initially followed by modest capacity fade. The cells with the best cycling performance at 55 °C contain standard electrolyte with capacities of over 160 mAh g⁻¹ and minimal fade. The LiDFOB in EC/DMC/DEC electrolyte also cycles well at 55 °C reaching just above 140 mAh g⁻¹ with

little fade upon cycling. The LiDFOB in GBL/MB electrolyte has a minor increase in capacity upon cycling at 55 °C with slightly greater capacity fade than is observed for the carbonate based electrolytes. However, the cycling performance of the LiDFOB in GBL/MB electrolyte is generally similar to the standard electrolyte and the slightly greater capacity fade upon cycling at 55 °C may be due to the lower purity of the LiDFOB and ester and lactone solvents compared to the very high purity of the battery grade LiPF_6 and carbonate solvents.

While there are performance differences in the various electrolyte formulations, they all have stable charge and discharge profiles as depicted for the 30th cycle in Figure 3.3. The standard electrolyte has slightly more capacity, but the LiDFOB formulations are similar.

Electrochemical Impedance Spectroscopy

The cells containing the different electrolytes are analyzed by electrochemical impedance spectroscopy (EIS) after the first 25 cycles at 16 °C as depicted in Figure 3.4, along with an equivalent circuit [34]. For the equivalent circuit, R_B represents the bulk resistance of the cell, R_{SL} represents the resistance of the surface layer including the SEI while C_{SL} represents the capacitance of the surface layer and is the response to high AC frequencies, R_{CT} represents the Faradaic charge transfer resistance with C_{DL} representing a double layer capacitance and are at mid-range frequencies, while W is representative of the Warburg impedance at low frequencies [34]. As related to the EIS plots, the first semicircle at lower resistance can be attributed to the high frequencies, the second

semicircle can be attributed to medium range frequencies, and the Warburg impedance is the straight line at a near 45° angle and is at low frequencies. The impedance is smallest for the cell cycled with the standard electrolyte followed by the cell containing the LiDFOB in EC/DEC/DMC electrolyte while the cell containing the LiDFOB in GBL/MB electrolyte has the highest impedance. The changes in impedance are primarily related to changes in the surface layer and charge transfer resistances and may result from changes in the structure of the SEI as discussed below.

Scanning Electron Microscopy

SEM images were acquired for both the anodes and cathodes extracted from cycled cells. Significant differences are observed for the anode surfaces cycled with the standard electrolytes compared to the LiDFOB electrolytes (Figure 3.5). The fresh anode particles have clean edges, and the graphite particles are well defined. After cycling in standard electrolyte, the graphite edges become slightly less defined, and the surface is covered with a thin film. The anode cycled with LiDFOB in EC/DMC/DEC electrolyte has a much thicker surface film which thoroughly covers the graphite. The anode cycled with the LiDFOB in GBL/MB electrolyte also has a very thick surface film although it is thinner than that observed with the LiDFOB in EC/DMC/DEC electrolyte.

The SEM Images of the cathodes are depicted in Figure 3.6 revealing less changes in morphology than observed for the anodes. The cathode cycled with the standard electrolyte is very similar to the fresh cathode suggesting little reaction of the electrolyte with the cathode surface. However the cathodes cycled with either of the LiDFOB

electrolytes have a thin film on the surface of the cathode particles consistent with the reaction of the electrolyte on the cathode surface.

X-ray Photoelectron Spectroscopy

The surface of both the anodes and the cathodes, fresh and after 55 cycles at 16 °C, were investigated by XPS. The C 1s, F 1s, O 1s, B1s, and P2p element spectra of the anodes are provided in Figure 3.7 while the elemental concentrations of the XPS spectra are provided in Table 3.2. The fresh anode is dominated by carbon and fluorine from the graphite and the PVDF binder with low concentrations of oxygen due to the presence of oxygenated impurities on the surface of the graphite. Upon cycling with the standard electrolyte the concentration of F, O and P are increased while the concentration of C is decreased consistent with electrolyte decomposition on the anode surface. With both LiDFOB electrolytes the decrease in C concentration is similar to the standard electrolyte however the F concentration is also decreased and the O and B concentrations are increased. Again the changes are consistent with electrolyte decomposition on the anode surface. Interestingly, the elemental concentrations of the anode cycled with the LiDFOB in EC/DMC/DEC and the LiDFOB in GBL/MB are very similar.

The fresh anode contains C1s peaks at 284.3 eV characteristic of graphite and 286.2 and 290.6 eV for the PVDF binder. The corresponding F1s peak of PVDF is observed at 687.9 eV. The XPS spectra of the graphite anodes cycled with the standard electrolyte are similar to those previously reported [19]. The C1s spectrum contains new peaks at 287 and 290 eV characteristic of C-O and CO₃⁻ containing species. The O1s spectrum contains peaks at 531.8 and 533.7 eV characteristic of C-O and CO₃⁻ containing species.

The C1s and O1s data is consistent with the presence of lithium alkyl carbonates and Li_2CO_3 . The F1s spectrum contains a new peak at 685.0 eV characteristic of LiF and a small new weak peak at 134.6 eV in the P2p spectrum characteristic of $\text{Li}_x\text{PO}_y\text{F}_z$. However, the SEI is relatively thin since the peaks associated with PVDF are still observed in the C1s and F1s spectra. The XPS spectra of the surface of the anodes cycled with LiDFOB electrolytes are significantly different than the XPS spectra observed for the standard electrolyte. This is expected since it has been reported that LiDFOB is involved in SEI formation [1, 4, 23, 25, 26, 28]. However, the XPS spectra of the surface of the anode cycled with the LiDFOB in EC/DMC/DEC and the anode cycled with LiDFOB in GBL/MB are very similar. This suggests that reduction of LiDFOB is the dominant SEI forming reaction in both LiDFOB electrolytes. The C1s spectrum is dominated by a peak at 288.3 eV characteristic of C=O containing species such as lithium oxalate or other oxalate containing species. The corresponding oxalate peak is observed in the O1s spectrum at 531.9 eV. A strong peak associate with LiF is observed at 685.0 eV [14, 33]. In addition, there is a new peak in the B1s spectrum at 193 eV characteristic of B-O containing species [14, 33]. The B-O peaks occur at 533 eV and overlap with C-O peaks. The surface films for both LiDFOB electrolytes are thick since the peaks associated with the PVDF binder (291 eV C1s, and 688 eV F1s) are weak.

The XPS spectra of the cathodes cycled with different electrolytes are provided in Figure 3.8 while the elemental concentrations of the fresh and cycled cathodes are summarized in Table 3.3. The fresh cathode has a high concentration of C and F from the conductive carbon and PVDF binder and low concentrations of O and Ni from the metal oxide. Upon cycling with the standard electrolyte only small changes are observed in the

elemental concentrations consistent with small changes to the surface of the cathode. Much larger changes are observed with both LiDFOB electrolytes. The concentrations of C, F, and Ni are decreased while the concentrations of O and B are increased consistent with the formation of a cathode surface film composed of electrolyte decomposition products. The elemental surface concentrations of the two LiDFOB electrolytes are very similar suggesting similar surface film structure.

The fresh cathode has C1s peaks at 284.2 eV for the conductive carbon and at 285.7 and 290.2 eV for the PVDF binder. The related F1s peak for PVDF is observed at 687.7 eV. The O1s spectrum contains peaks at 531.3 and 528.7 eV characteristic of residual Li_2CO_3 on the surface and the metal oxide, respectively. The corresponding metal oxide peak is also observed in the Ni2p spectrum at 855.6 eV in the Ni2p spectrum. After cycling in the presence of the standard electrolyte only small changes are observed to the surface of the cathode. A new peak is observed in the F1s spectrum at 684.6 eV characteristic of LiF and the peak associated with the metal oxide (528 eV) in the O1s spectrum is slightly diminished consistent with the generation of a thin surface film. The surfaces of the cathodes cycled with both LiDFOB electrolytes have significant changes upon cycling. The C 1s spectra contain a new peak at 288 eV characteristic of lithium oxalate or other oxalates and the corresponding O1s peak is observed at 532.4 eV in the O1s spectrum. In addition, peaks are observed in the B1s spectra at 192.5 eV consistent with the presence of borates, as previously reported on the surface of cathodes cycled with LiDFOB or LiBOB [14, 28]. The cathode surface film is thinner than the SEI observed on the anodes cycled with the LiDFOB electrolytes, since the peaks associated with the PVDF binder are still observable at 290.5 and 286 eV, but thicker than the

surface film observed on the cathode cycled with the standard electrolyte since the peak associated with the metal oxide is no longer observable.

Infra-Red Spectroscopy

The anodes and cathodes extracted for cells cycled with different electrolytes were investigated by IR-ATR spectroscopy (Figure 3.9 and Figure 3.10). The fresh anode contains absorptions characteristic of PVDF at 870, 1410, and 1500 cm^{-1} [14, 30, 35]. The spectrum for the anode cycled with the standard electrolyte is very similar to that of the fresh anode, except there is a new weak absorption at 1600 cm^{-1} consistent with the presence of lithium alkyl carbonates and a strong absorption at 1420 cm^{-1} characteristic of Li_2CO_3 . The IR spectra of the anodes cycled with the LiDFOB electrolytes are very similar to each other, and different from the IR spectra of the anode cycled with the standard electrolyte. New peaks are observed at 1630 and 1760 cm^{-1} characteristic of lithium oxalates and oligocarbonates, respectively [29].

The IR spectrum of the fresh cathode is dominated by the peaks associated with the PVDF binder. The IR spectrum of the cathode cycled with the standard electrolyte is also dominated by the PVDF binder. The IR spectra of the cathodes cycled with the LiDFOB electrolytes have new absorptions at 1630 and 1760 cm^{-1} consistent with the presence of lithium oxalates and oligocarbonates, respectively [29].

Conclusions

A novel electrolyte formulation without any LiPF_6 or carbonate solvents has been developed and investigated in lithium ion batteries. The 1 M LiDFOB in GBL/MB electrolyte has comparable ionic conductivity and room temperature cycling performance to the industry standard electrolyte, 1 M LiPF_6 in 1:1:1 EC/DMC/DEC. Cells containing the LiDFOB in GBL/MB electrolyte also have a slightly decreased discharge performance at $-10\text{ }^\circ\text{C}$ and have good capacity retention upon cycling at $55\text{ }^\circ\text{C}$, to simulate accelerated aging. Cells containing the LiDFOB in GBL/MB electrolyte have slightly higher impedance than cells cycled with the standard electrolyte. The slightly decreased capacity at low temperature is in contrast to the superior conductivity at low temperature and is likely due to the increased cell impedance due to changes in the structure of the SEI. Thus upon developing new electrolytes it is important to analyze both the bulk properties of the electrolyte and the interfacial reactions of the electrolyte with the electrode materials.

Ex-situ surface analysis provides insight into the role of the LiDFOB salt in SEI formation and cell cycling performance. XPS and IR spectroscopy confirm that the structure of the anode SEI is dominated by the decomposition products of LiDFOB. The anode SEI generated for both the LiDFOB in GBL/MB electrolyte and the LiDFOB in EC/DMC/DEC electrolyte have nearly identical structure. The anode SEI is dominated by the presence of lithium oxalate, other oxalate containing species, and borates and is much thicker than the anode SEI generated with the standard electrolyte. The surface films on the cathodes cycled with the LiDFOB electrolytes have similar structure to the anode SEI and are thicker than the surface films generated on the cathode cycled with the

standard electrolyte. The thick surface films composed of the decomposition products of LiDFOB passivate the surface of the anode and enable stable cycling performance in the presence of the all ester electrolyte. Depending upon the electrolyte the reduction products of either the salt or the solvent can dominate the structure of the SEI.

Acknowledgements

We thank Optodot and the US Department of Energy grant number DE-EE0005433 for funding, BASF for providing electrolyte, and Yardney Technical products for providing electrodes and separators.

References

- [1] V. Aravindan, J. Gnanaraj, S. Madhavi, and H-K Liu, *Chem. Eur. J.*, **17**, 14326 (2011).
- [2] J.B. Goodenough and K-S Park, *J. Am. Chem. Soc.*, **135**, 1167 (2013).
- [3] V. Etacheri, R. Marom, R. Elazari, G. Salitra, and D. Aurbach, *Energy Environ. Sci.*, **4**, 3243 (2011).
- [4] S.S. Zhang, *Electrochem. Commun.*, **8**, 1423 (2006).
- [5] K. Xu, *Chem. Rev.*, **104**, 4303 (2004).
- [6] C.L. Campion, W. Li, and B.L. Lucht, *J. Electrochem. Soc.*, **152**, A2327 (2005).
- [7] W. Li, C. Campion, B. L. Lucht, B. Ravdel, and K. M. Abraham, *J. Electrochem. Soc.*, **152**, A1361 (2005).
- [8] S. E. Sloop, J. B. Kerr, and K. Kinoshita, *J. Power Sources*, **119-121**, 330 (2003).
- [9] K. Xu, Y. Lam, S.S. Zhang, T.R. Jow, and T.B. Curtis, *J. Phys. Chem. C*, **111**, 7411 (2007).
- [10] M. Nie, D. Chalasani, D.P. Abraham, Y. Chen, A. Bose, and B.L. Lucht, *J. Phys. Chem. C*, **117**, 1257 (2013).
- [11] P. Verma, P. Maire, and P. Novák, *Electrochim. Acta*, **55**, 6332 (2010).
- [12] P. Lu, C. Li, E.W. Schneider, and S.J. Harris, *J. Phys. Chem. C*, **118**, 896 (2014).
- [13] K. Xu, *Energies*, **3**, 135 (2010).
- [14] M. Nie and B.L. Lucht, *J. Electrochem. Soc.*, **161**, A1001 (2014).
- [15] M.C. Smart, B.V. Ratnakumar, K.B. Chin, and L.D. Whitcanack, *J. Electrochem. Soc.*, **12**, A1361 (2010).
- [16] S. Li, W. Zhao, X. Cui, Y. Zhao, B. Li, H. Zhang, Y. Li, G. Li, X. Ye, and Y. Luo, *Electrochim. Acta*, **91**, 282 (2013).
- [17] K. Xu, S.S. Zhang, and T.R. Jow, *J. Electrochem. Solid-State Lett.*, **5**, A26 (2002).
- [18] K. Xu, *J. Electrochem. Soc.*, **155**, A733 (2008).
- [19] Z. Zhang, L. Hu, H. Wu, W. Weng, M. Koh, P.C. Redfern, L.A. Curtiss, and K. Amine, *Energy Environ. Sci.*, **6**, 1806 (2013).

- [20] W. Xu, A.J. Shusterman, M. Videa, V. Velikov, R. Marzke, and C.A. Angell, *J. Electrochem. Soc.*, **150**, E74 (2003).
- [21] Y. Yamada, K. Usui, C.H. Chiang, K. Kikuchi, K. Furukawa, and A. Yamada, *Appl. Mater. Interfaces*, **6**, 10892 (2014).
- [22] D.W. McOwen, D.M. Seo, O. Borodin, J. Vatamanu, P.D. Boyle, and W.A. Henderson, *Energy Environ. Sci.*, **7**, 416 (2014).
- [23] S.S. Zhang, *J. Power Sources*, **163**, 713 (2007).
- [24] S. Zugmann, M. Fleischmann, M. Amereller, R.M. Gschwind, M. Winter, and H.J. Gores, *J. Chem. Eng. Data*, **56**, 4786 (2011).
- [25] M.H. Fu, K.L. Haung, S.Q. Liu, J.S. Liu, and Y.K. Li, *J. Power Sources*, **195**, 862 (2010).
- [26] I.A. Shkrob, Y. Zhu, T.W. Marin, and D.P. Abraham, *J. Phys. Chem. C*, **117**, 23750 (2013).
- [27] H. Zhou, Z. Fang, and J. Li, *J. Power Sources*, **230**, 148 (2013).
- [28] M. Xu, L. Zhou, L. Hao, L. Xing, W. Li, and B.L. Lucht, *J. Power Sources*, **196**, 6794 (2011).
- [29] M. Xu, A. Xiao, W. Li, and B. L. Lucht, *J. Electrochem. Soc.*, **157**, A115 (2010).
- [30] L. Zhou and B.L. Lucht, *J. Power Sources*, **205**, 439 (2012).
- [31] D. Belov and D.T. Shieh, *J. Solid State Electrochem.*, **16**, 603 (2012).
- [32] J. Kestin, M. Sokolov, W.A. Wakeham, *J. Phys. Chem. Ref. Data*, **7**, 941 (1978).
- [33] E.A. Il'inchik, V.V. Volkov, and L.N. Mazalov, *J. Struct. Chem.*, **46**, 523 (2005).
- [34] S.S. Zhang, K. Xu, T.R. Jow, *J. Power Sources*, **115**, 137, (2003).
- [35] T. Boccaccio, A. Bottino, G. Capannelli, and P. Piaggio, *J. Membr. Sci.*, **210**, 315 (2002).

Figures and Tables

Figure 3.1

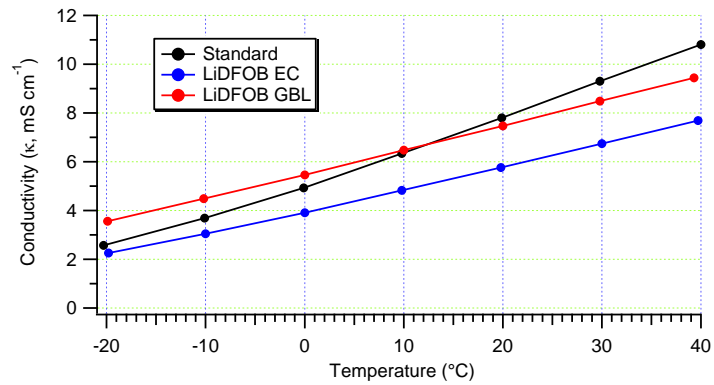


Figure 3.1: Conductivity measurements of the electrolyte systems used in the cells above.

Figure 3.2

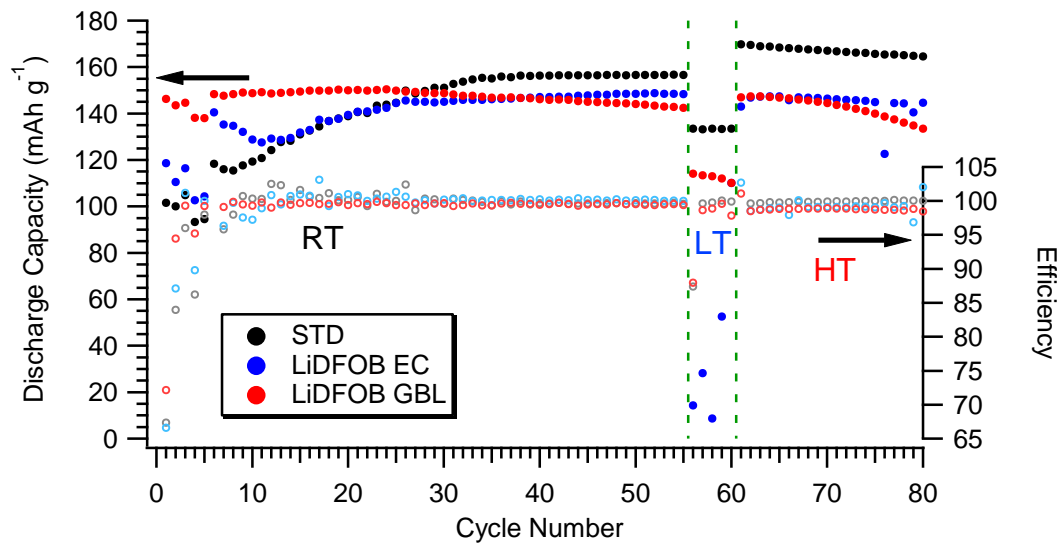


Figure 3.2: Cycling performance for various electrolyte formulations. The first 55 cycle are at room temperature (RT, 16° C), the next five are at low temperature (LT, -10° C), and the last 20 are at high temperature (HT, 55° C).

Figure 3.3

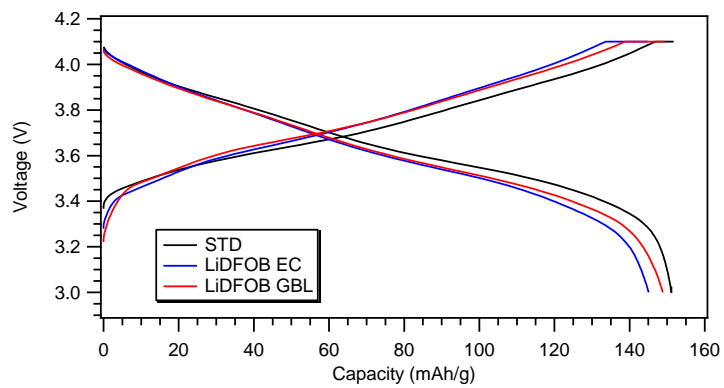


Figure 3.3: Charge/Discharge plot of the best cells at cycle 30.

Figure 3.4

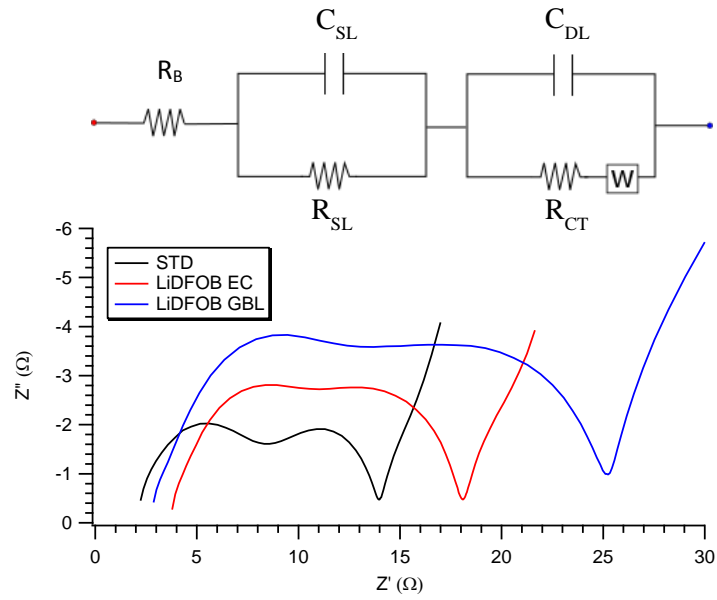


Figure 3.4: Electrochemical impedance spectroscopy after 25 cycles, including formation, along with a representative circuit [34]. EC denotes LiDFOB/EC/DMC/DEC electrolyte formulation and GBL denotes LiDFOB/GBL/MB formulation.

Figure 3.5

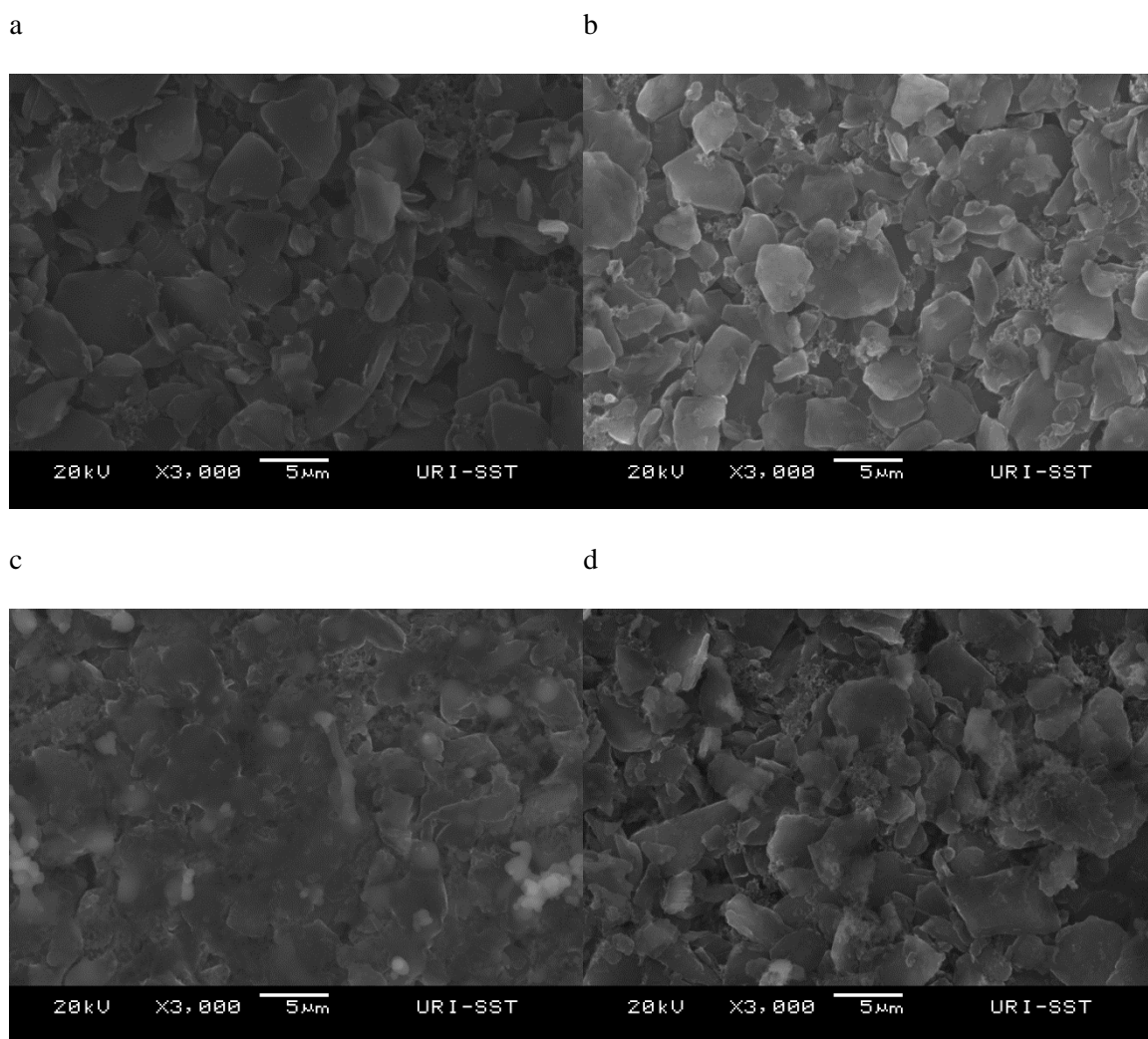


Figure 3.5: SEM images for anode of [a]: Fresh [b]: Standard [c]: LiDFOB in EC/DMC/DEC and [d]: LiDFOB in GBL/MB. These samples were taken from the best performing samples and are secondary electron images.

Figure 3.6

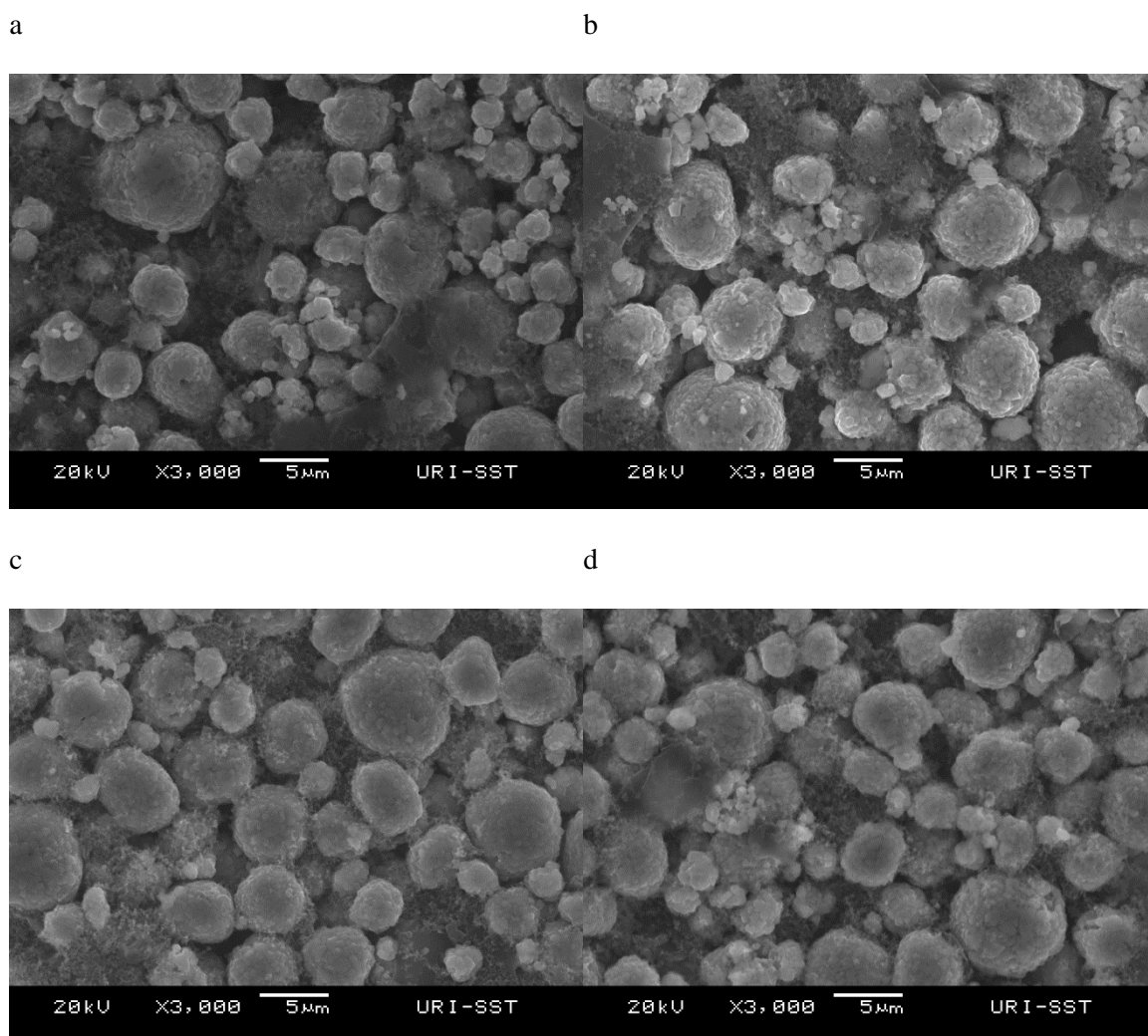


Figure 3.6: SEM images for cathode of [a]: Fresh [b]: Standard [c]: LiDFOB in EC/DMC/DEC and [d]: LiDFOB in GBL/MB. These samples were taken from the best performing samples and are secondary electron images.

Figure 3.7

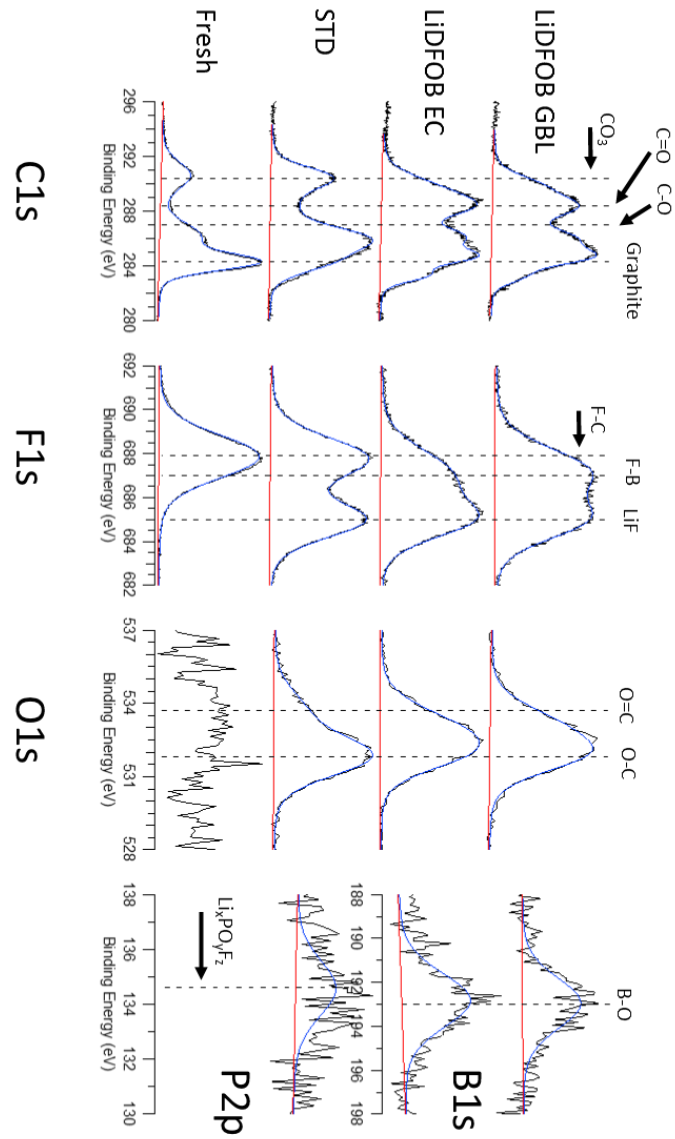


Figure 3.7: XPS spectra of the anode extracted from cells cycled with the three different electrolyte formulations. From left to right, the spectra are C 1s, F 1s, O 1s, and B 1s/P2p. From bottom to top is fresh anode, standard electrolyte, LiDFOB in EC/DMC/DEC, and LiDFOB in GBL/MB.

Figure 3.8

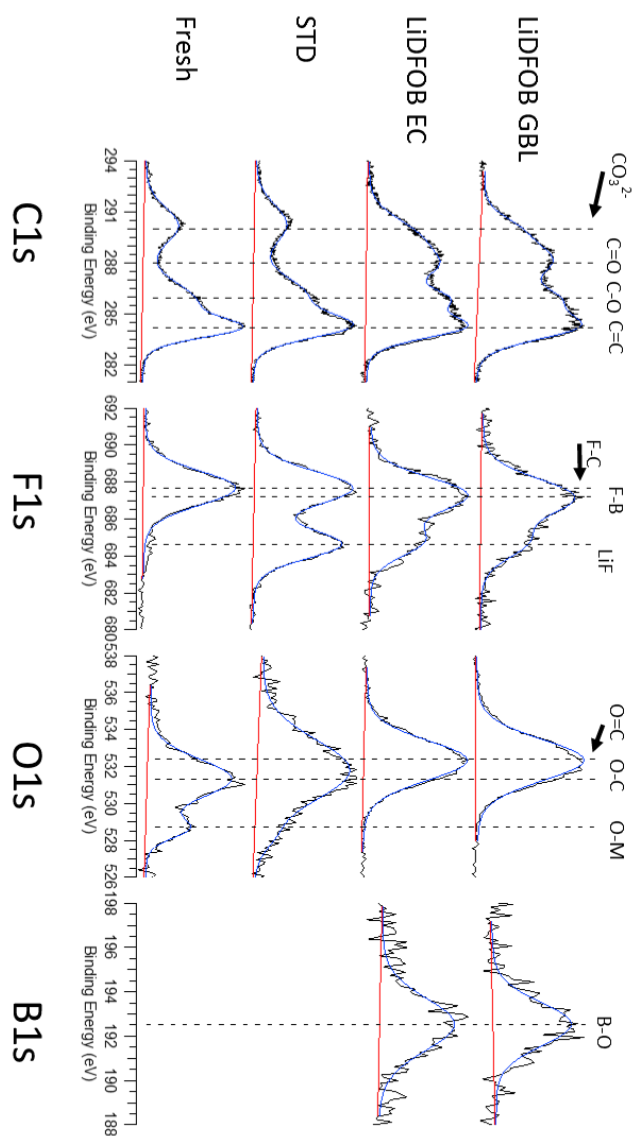


Figure 3.8: XPS spectra of the cathodes cycled with the different electrolyte formulations. From left to right, the spectra are C 1s, F 1s, O 1s, and B 1s. From bottom to top is fresh cathode, standard electrolyte, LiDFOB in EC/DMC/DEC, and LiDFOB in GBL/MB.

Figure 3.9

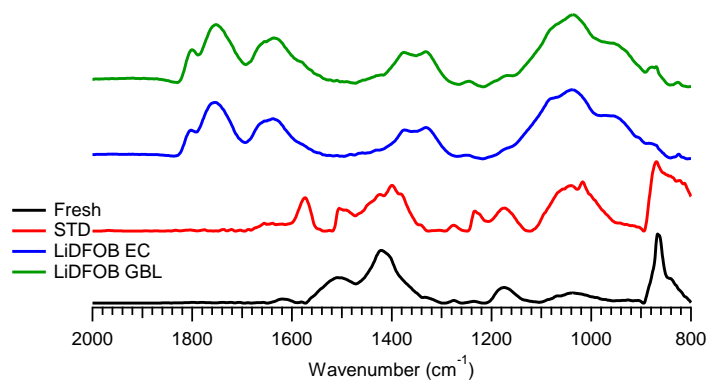


Figure 3.9: FTIR-ATR spectra of anodes.

Figure 3.10

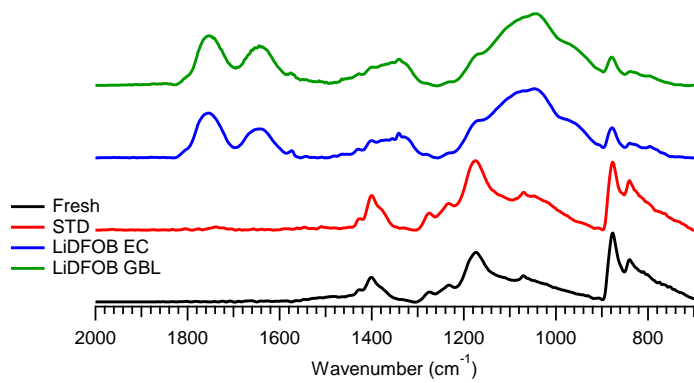


Figure 3.10: FTIR-ATR of cathode samples.

Table 3.1

	STD	LiDFOB
		GBL
Density (g/mL)	1.21	1.09
Viscosity (mPa s, cP)	3.57	2.94
Error (%)	0.1	0.6

Table 3.1: Viscosity of the standard electrolyte and the LiDFOB in GBL/MB electrolyte.

Table 3.2

Sample	[B] %	[C] %	[F] %	[O] %	[P] %
<i>Fresh</i>	0.0	68.5	30.6	0.8	0.0
<i>Standard</i>	0.0	44.8	42.1	12.6	0.5
<i>LiDFOB-EC</i>	4.5	48.5	23.1	23.9	0.0
<i>LiDFOB-GBL</i>	3.7	49.1	24.0	23.2	0.0

Table 3.2: Relative concentration of elements on the surface of the anodes from XPS.

Table 3.3

Sample	[B] %	[C] %	[F] %	[O] %	[Ni] %
<i>Fresh</i>	0.0	70.8	16.2	9.9	3.0
<i>Standard</i>	0.0	63.4	24.7	9.4	2.5
<i>LiDFOB-EC</i>	4.8	56.7	10.5	26.6	1.4
<i>LiDFOB-GBL</i>	5.1	55.1	9.0	29.9	1.0

Table 3.3: Relative concentration of elements on the surface of the cathodes from XPS.

Chapter 4 - Comparison of Ceramic Containing and Polyolefin Separator Performance in Lithium Ion Batteries

Michael L. Lazar, Brett L. Lucht

Abstract

A separator consisting of a polyolefin and ceramic blend is compared to a standard polyolefin. Coin cells are built using these separators and cycled for 200 plus cycles at 55° C and monitored for capacity fade. Upon performance differences, surviving cells cycled at a [C/5] rate were analyzed by XPS and FTIR-ATR to look for differences in the SEI. Of the surviving cells that cycled at the [C/5] rate versus the [C/2] rate, the two sets have contradicting results with the [C/5] cells showing the MTI cell outlasting the standard cell while the [C/2] shows the standard cells outlasting the MTI cells.

Introduction

Electric Vehicles (EV) are being pursued by auto makers around the world, and this is drawing interest in better, longer lasting lithium ion batteries [1]. The interest of longevity is rooted in the need for the battery to have a long cycle life and a long calendar life for large format batteries used in EV or other large applications. Both the separator and the electrolyte play a key role in the longevity of the battery.

The role of the separator in the battery is to keep apart the anode and cathode to prevent electrical shorting, but this barrier affects the migration of the lithium ions between the electrodes by adding resistance. The separator may also add moisture or impurities to the electrolyte but may also remove them from the electrolyte; the latter has been difficult to demonstrate experimentally. Many researchers have investigated a variety of separator technologies that include plastics, ceramic coated plastics, and ceramic separators [2-7]. While many researchers investigate new separator technologies, they often compare their novel separators to some standard, usually a polyolefin, but they do not analyze cell performance beyond basic cycling of their separator, and there is no published research that looks into why certain separators work better than others [3-7]. Most of these papers point to better performance of ceramic containing separators over polyolefin, but the reasons are not thoroughly investigated. It is important to identify why one type of separator provides better longevity than another to help focus further research with regards to the separator and the electrolyte.

To look for these differences, it is necessary to investigate how the separator effects the solid electrolyte interface (SEI), as the SEI has great influence over the performance of the battery [8-13]. The SEI forms both organic reduction products and lithium salts on the anode [9, 10, 13]. One salt that is seen in particular is lithium fluoride (LiF), and this is in part caused by impurities in the electrolyte, especially water [14, 15]. LiPF_6 exists in equilibrium with LiF and PF_5 . Water reacts with PF_5 to create HF and fluorophosphates, which can continue to break down the electrolyte, especially at elevated temperatures, and creates more LiF when PF_5 is consumed [8, 14, 15]. The separator, especially one that has ceramic components, can introduce water to the

electrolyte, thus influencing the $\text{LiPF}_6/\text{PF}_5$, LiF equilibrium and making LiF salt that can end up in the SEI. This consumption of lithium along with the possibility of a denser SEI can impact conductivity and capacity retention of the cell [9, 10]. Thus, the success or failure of ceramic based separators hinges on the ability of the ceramics to keep any water it has from entering the electrolyte, capturing any water that might exist in the electrolyte, or capturing any HF that is in the electrolyte, and to do this more effectively than the polyolefin separator.

Cells containing the ceramic/polyolefin separator will thus be compared to cells containing a standard polyolefin separator. Cells will also undergo EIS to keep track of resistance. Upon a performance difference, the cells will be opened and examined by XPS and FTIR. Over the long term, this should give a representation of how cells with ceramic in the separator compares to only a polyolefin separator.

Experiment

A standard polyolefin (polyethylene, Setela E20MMS, 20 μm thick) and a 16 μm thick MTI brand (EQ-bsf-0016-500A) using aluminum oxide double coated polyethylene are compared. All separators were dried in a vacuum oven at 60° C for at least three days before use. Multiple 2032 coin cells were prepared with an anode composed of G5 graphite (89% G5 Graphite, 2% Super P carbon, 8.9% PVdF, 0.1% adhesive enhancer) and a cathode composed of $\text{LiNi}_{0.80}\text{Co}_{0.15}\text{Al}_{0.05}\text{O}_2$ (89% LNMAO, 2% KS15 graphite, 2% SAB, 2% Super P carbon, 5% PVdF) and were provided by Yardney Technical Products. The electrolyte used was 1 M LiPF_6 in 1:1:1 EC/DMC/DEC by weight and was provided by BASF.

The cells were cycled at 25° C (room temperature, RT) for formation cycling and an additional ten [C/5] cycles for conditioning and to make sure that the cells were good enough to continue cycling. One set of cells cycled at 55° C (high temperature, HT) at [C/5] for 200 cycles, while a second set cycled at 55° C at [C/2] for 300 cycles. For the HT [C/5] cells, the 200 cycles were broken into two sets of 100 because it was unknown how long it would take to see differences and did not want to risk running the cells to eventual failure. This incremental approach was taken to help monitor the cells progress and to take EIS measurements after 200 HT cycles. The [C/2] cells cycled for an initial 200 cycles and then for 100 more to find differences. Formation cycling includes one [C/20], two [C/10], and two [C/5] cycles. Each cycle rate is based off the theoretical capacity of the cell, and each cycle includes a constant current charge up to 4.1 V followed by a constant voltage charge until 10% of the current rate is reached. Cell are discharged at constant rate, and there are 20 minute rest periods between charging and discharging. When cells went from room temperature cycling to high temperature cycling, they were allowed to sit for four hours to ensure they start cycling at HT.

Cycling performance is evaluated by specific capacity at elevated temperature. Capacity will be determined by dividing the discharge capacity by the mass of the active material of the cathode, which is the limiting factor for these cells.

Electrochemical impedance spectroscopy (EIS) was conducted on cells after 200 cycles at 55° C with a BioLogic VSP using EC-Lab V10.37 software. Cells were charged at a C/5 rate to 4.1 V followed by holding at constant voltage for 10 hours. For EIS measurements, the cells were held again at constant voltage of 4.1V for a half hour, and EIS was taken from 300 kHz to 20 mHz. Cells were then discharged at a [C/5] rate.

Cells were opened in an argon filled glove box and washed three times with anhydrous DMC to remove the electrolyte and then dried overnight at room temperature under vacuum for surface analysis. FTIR-ATR (Fourier Transform Infrared Spectroscopy – Attenuated Total Reflectance) was acquired with a Bruker TENSOR 27 spectrometer with a germanium crystal and ATR accessory, and was purged continuously with nitrogen. Samples were analyzed at two separate locations on the electrode from 700 to 4,000 cm^{-1} with 128 scans.

XPS (X-ray Photoelectron Spectroscopy) was conducted with a K-Alpha Surface Analysis from Thermo Fisher system using Al $K\alpha$ radiation source ($h\nu = 1486 \text{ eV}$) under ultrahigh vacuum. The resolution is 50 meV and the pass energy was 50 eV to minimize beam exposure to the sample (the beam can cause reactions that can alter the chemical composition of the surface, so a higher pass energy allows for shorter exposure times while getting decent readings at the expense of slight peak broadening). The spectra were analyzed and manipulated using Thermo Avantage V5.932 software. For XPS samples, two spots were taken on each sample for better sample representation.

Results

Cycling

After undergoing an abusive 200 [C/5] cycles at 55° C, one standard and one MTI cell, which performed similarly for most of this experiment finally differentiated around HT cycle 140. After this point, the standard cell began a non-linear decline in capacity while the MTI cell maintained a linear decline, suggesting that the ceramic containing separator

can have a performance advantage over a polyolefin separator (Figure 1). These were the only cells to survive to this point in this set out of three standards and four MTI cells.

At the beginning of HT cycling, both the standard and the MTI cells have a small capacity dip, which may be caused by the dissolving of the SEI. This may happen at high temperature because the SEI salts may have some solubility in the warmer electrolyte that they did not have at cooler temperatures. The dissolution can take back some of the lithium helping to boost the capacity in exchange for more organic SEI components.

At cycle 101, the MTI shows a capacity boost, while the standard does not. This capacity boost is caused because of a short break after 100 HT cycles.

For the cell cycling at [C/2], two out of three standard and two out of four MTI cells made it to 300 HT cycles. The successful cells are displayed in Figure 4.2. The [C/2] standards cycled much like the cells in the [C/5] experiment, where there is a dip in capacity followed by a slight increase in capacity before a long fade. The MTI cells however did not follow this pattern, they started to fade from the beginning. This behavior difference can account for the capacity differences between the MTI and the standard cells. As the cells approach the 200th cycle, the MTI appears as if it will outlast the standard, but it does not as the cells reach 200 cycles. After a layoff of at least a few days and EIS experiments on the cells, the cells resume HT cycling with all cells experiencing a small dip in capacity. After resuming, cell MTI 2 experiences a nonlinear decline, with MTI 1 following the standard cells until the last ten to twenty cycles approaching 300 HT cycles. The standard cells experience only linear decline. Thus for the cells cycling at [C/2], the standard cells appear to outperform the MTI cells.

Electrochemical Impedance Spectroscopy (EIS)

All cells that were able to cycle to 200 HT cycles are examined by EIS. In addition, new cells are examined by EIS only after formation to get a comparison of the resistance profile before and after extensive and abusive cycling. The data in figure 4.3 and 4.4 clearly demonstrates the increase in resistance in the cells. Additionally, the spectra shape shows two clear semi circles after the HT cycling for the [C/5] and the [C/2] cells, whereas the cells after formation have spectra that show un-resolved semi circles. This is an indication that as the cells age, the resistance due to bulk lithiation begins to separate from the resistance due to the SEI. Both SEI resistance and bulk resistance increase as the cells age. What is also clear from the spectra, is that when cells begin to fail, the impedance increases. The performance deviation shows for the [C/5] cells that the impedance for the MTI cell is clearly lower than that of the standard, but they are roughly the same for the [C/2] cells when performance is similar.

XPS Analysis

XPS analysis was done on fresh anode and cathode and the surviving MTI and standard cells that underwent 200 HT cycles at a [C/5] rate. For the anode, C1s, F1s, O1s, Li1s, and P2p was taken and for the cathode, the same elements were taken along with Co2p, Al2p, and Ni2p. The C1s, F1s, O1s, and P2p are provided in figures 4.5 and 4.6 for the anode and the cathode. The tables containing the elemental concentrations are provided in tables 4.1 and 4.2.

The anode elemental concentrations between the standard cells and the MTI cells are inconsistent considering that they use the same electrolyte, but it is important to note that the standard cell shows significantly more fade by the end of the 200th HT cycle. The concentration of F and O changes from the fresh to the MTI and standard cells, where O rises and F drops. The concentration of C stays roughly the same between the fresh and MTI cell, but drops between the fresh and the standard cell. The P concentration between the standard and MTI cells is consistent around 3%.

The XPS analysis of the anode shows peaks for C1s at 286.2 and 290.7 eV characteristic of the C-H and C-F bonds from PVDF binder respectively. These peaks persist in the cycled samples as well, but they shift to lower energy, where carbonate species are present. The peak at 284.3 eV in the fresh sample is representative of graphite carbon, and the peak exists in the cycled samples, but broadens due to SEI species, particularly C-O peaks at 287 eV, and C=O peaks at 288.3 eV. The F1s spectra show the F-C peak from PVDF at 687.9 eV, and this peak does exist in the cycled samples as well, but the peak shifts slightly to lower energy indicating other fluorine species, most likely fluorophosphates. The O1s spectra does not look too different between the fresh sample and the cycled samples other than intensity. The fresh sample most likely has C=O character, while the cycled samples show more of a mix of C=O at 532.7 eV and C-O at 531.3 eV. The MTI shows a peak around 528 eV which can be characteristic of lithium oxide forming from beam damage or from residual ceramics transferred from the separator. Lastly, the P2p spectra shown on the standard and MTI samples is highly present and is representative of lithium fluorophosphate species. Overall, it appears that

the anode SEI for both cycled samples has a lot of carbon and oxygen content, and it is likely that that is a combination of salts with lithium and polycarbonates.

For the cathode, the elemental concentrations change from the fresh to the cycled samples. The concentration differences between the standard and MTI samples are similar, so the performance fade of the standard cell is not rooted in the cathode. For both cycled samples as compared to the fresh sample, the concentration of carbon decreases while the concentration of oxygen increases. Fluorine stays constant. The changes in C and O are consistent with the formation of polycarbonates, which are clearly present in the FTIR data that will be described in the next section.

Like the anode, the cathode shows similar peaks. PVDF peaks from the fresh sample are similar to those described for the anode with C1s peaks at 290.7 eV and 286.2 eV and F1s peak at 687.9 eV indicating PVDF. There is a clear intensity increase in the C1s spectra for the cycled samples around 290.2 eV consistent with carbonates, and the carbon peaks near 284.3 eV consistent with graphite and C=C bonds broadens indicating more carbon oxygen species on the cathode surface. LiF is clearly present at 685 eV in the F1s spectra, even in the fresh sample, which is commonly seen. The O1s spectra shows a decrease in the oxygen-metal peak that is presumably covered by the polycarbonates, and the peak broadens between 535 to 530 eV to include various carbon-oxygen species including carbonates. Lastly, much like the anode, there are lithium fluorophosphates present in the cathode with the P2p spectra for the cycled samples showing a peak at 134.8 eV.

FTIR Analysis

FTIR-ATR analysis was done for both the MTI cell and standard cell and is compared to a fresh, uncycled electrode. For the anode, shown in figure 4.7, PVDF shows at 870, 1410, and 1500 cm^{-1} , and can be seen to some extent on the cycled samples. The spectra for the MTI cell and the standard cell look the same, and have peaks showing at 1030, 1440, 1580, and 1740 cm^{-1} . The large peak at 1030 cm^{-1} is carbon-oxygen species, the peak at 1440 cm^{-1} is characteristic of lithium carbonate, the peak at 1580 cm^{-1} is characteristics of lithium alkyl carbonates, and the small set of peaks at 1740 cm^{-1} are from small amounts of polycarbonates.

The cathode FTIR-ATR spectra, shown in figure 4.8, shows PVDF binder at 870, 1410, and 1500 cm^{-1} . The spectra are largely similar for all the samples, but the cycled samples show a big peak at 1740 cm^{-1} which can be attributed to polycarbonates. The MTI cell and the standard cell have similar spectra indicating no difference in cathode electrolyte interface make-up on the cathode.

Conclusions

Cells containing standard polyolefin separators and a ceramic coated polyolefin separator are cycled and analyzed to understand any advantages ceramics may have in lithium ion cells. The cells that cycle at a [C/5] rate for 200 HT cycles show that the MTI cell outlasts the standard cell, but the cells that cycle at the [C/2] show that the standard outlasts the MTI. However, there is some indication in the [C/2] cells that suggest that

the MTI cells can outlast the standard cells as the steady decline of the MTI is not as sharp as the faster decline of the standard before HT cycle 200. Had the cells not been stopped at HT cycle 200 and allowed to continue, the MTI cells may have outlasted the standard barring any sudden rapid fading. Another complication for the [C/2] cells is that the MTI started HT cycling near its peak capacity while the standard declines, and then increases making its peak capacity near the 60th HT cycle, which gives it an advantage as far as capacity is concerned over the course of the experiment. This cycling inconsistency could have interfered with the experiment. EIS shows that neither the standard or the MTI cells have an advantage of resistance after much HT cycling with the exception of the [C/5] cells where the MTI has slightly less resistance, but that is due to quick performance fade of the standard cell. The ex-situ analysis of the [C/5] cells show almost no difference in the XPS and the FTIR-ATR spectra, with the only difference in the elemental concentrations for the anode of the standard cell due to the failure of the cell. Considering that the performance differences between the standard cell and the MTI cell are not quite clear, the possibility should be open that ceramic contents in the separator may not have an effect on cell performance over the long term. To better gauge differences in long term cell performance between polyolefin and ceramic containing separators, better cells will have to be built that can last hundreds of cycles without a high failure rate which is commonly seen with coin cells.

Acknowledgements

Special thanks to Optodot for funding (under U.S. Department of Energy grant DE-EE0005433) and for the ceramic separators used for this experiment, Yardney for the electrodes and the Setela polyolefin separators, and BASF for the electrolyte.

References

- [1] Vehicle Technologies Office: 2013 Energy Storage R&D Progress Report, Department of Energy. <http://energy.gov/eere/vehicles/downloads/vehicle-technologies-office-2013-energy-storage-rd-progress-report-sections> (Accessed 01 Oct. 2014).
- [2] S.S. Shang, *J. Power Sources*, **164**, 351 (2007).
- [3] W.K. Shin, D.W. Kim, *J. Power Sources*, **226**, 54 (2013).
- [4] D. Fu, B. Luan, S. Argue, M.N. Bureau, I.J. Davidson, *J. Power Sources*, **206**, 325 (2012).
- [5] T.H. Cho, M. Tanaka, H. Ohnishi, Y. Kondo, M. Yoshikazu, T. Nakamura, T. Sakai, *J. Power Sources*, **195**, 4272 (2010).
- [6] H.S. Jeong, S.Y. Lee, *J. Power Sources*, **196**, 6716 (2011).
- [7] J.A. Choi, S.H. Kim, D.W. Kim, *J. Power Sources*, **195**, 6192 (2010).
- [8] K. Xu, *Chem. Rev.*, **114**, 11303 (2014).
- [9] P. Lu, C. Li, E.W. Schneider, S.J. Harris, *J. Phys. Chem. C*, **118**, 896 (2014).
- [10] M. Nie, D. Chalasani, D.P. Abraham, Y. Chen, A. Bose, and B.L. Lucht, *J. Phys. Chem. C*, **117**, 1257 (2013).
- [11] K. Xu, *Energies*, **3**, 135 (2010).
- [12] M. Nie and B.L. Lucht, *J. Electrochem. Soc.*, **161**, A1001 (2014).
- [13] K. Xu, Y. Lam, S.S. Zhang, T.R. Jow, and T.B. Curtis, *J. Phys. Chem. C*, **111**, 7411 (2007).
- [14] C.L. Campion, W. Li, and B.L. Lucht, *J. Electrochem. Soc.*, **152**, A2327 (2005).

[15] S. E. Sloop, J. B. Kerr, and K. Kinoshita, *J. Power Sources*, **119-121**, 330 (2003).

Figures

Figure 4.1

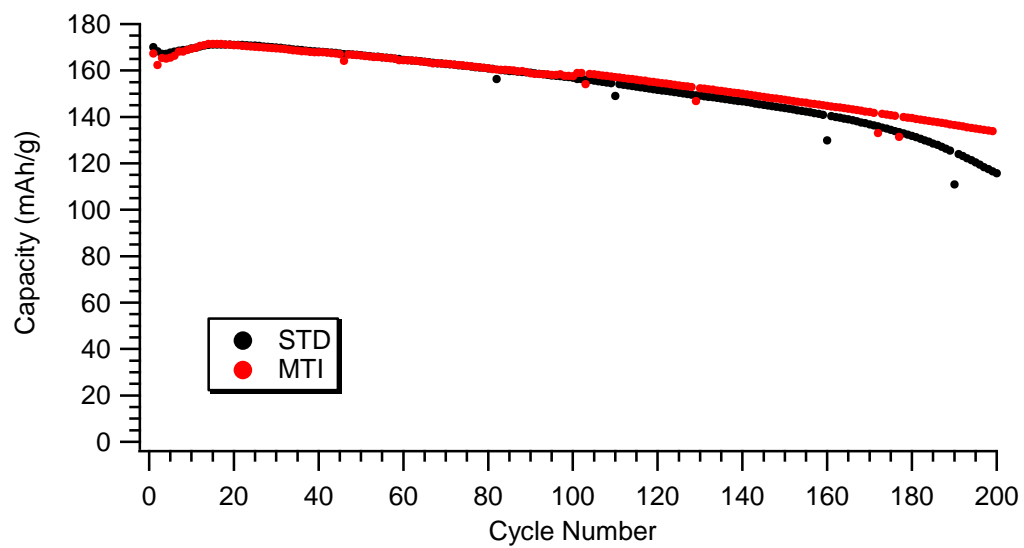


Figure 4.1: 200 [C/5] cycles at HT for the only surviving standard and MTI cells.

Figure 4.2

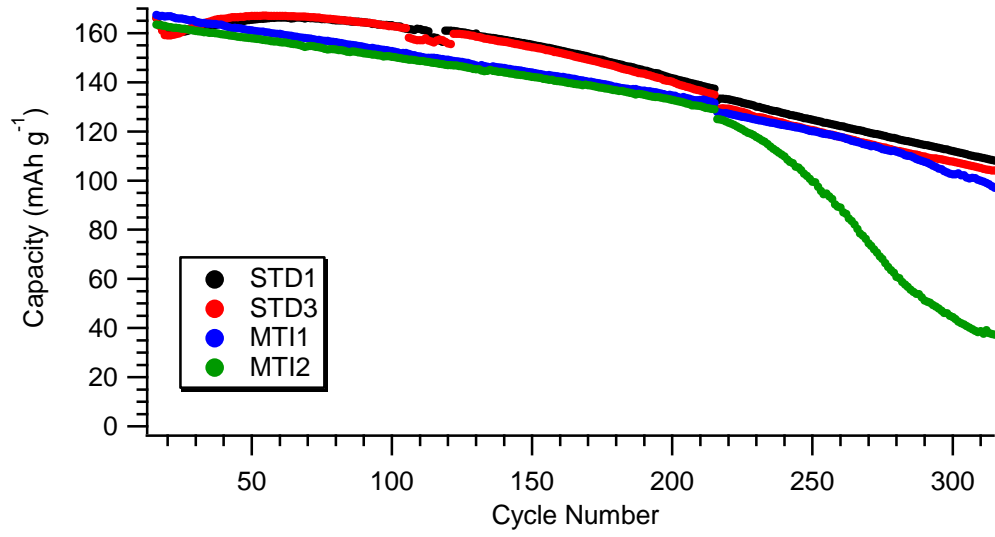


Figure 4.2: MTI and standard cells cycled at 55° C for 300 cycles at a [C/2] rate. The profile is slightly different than the profile for the same cell types cycled at [C/5].

Figure 4.3

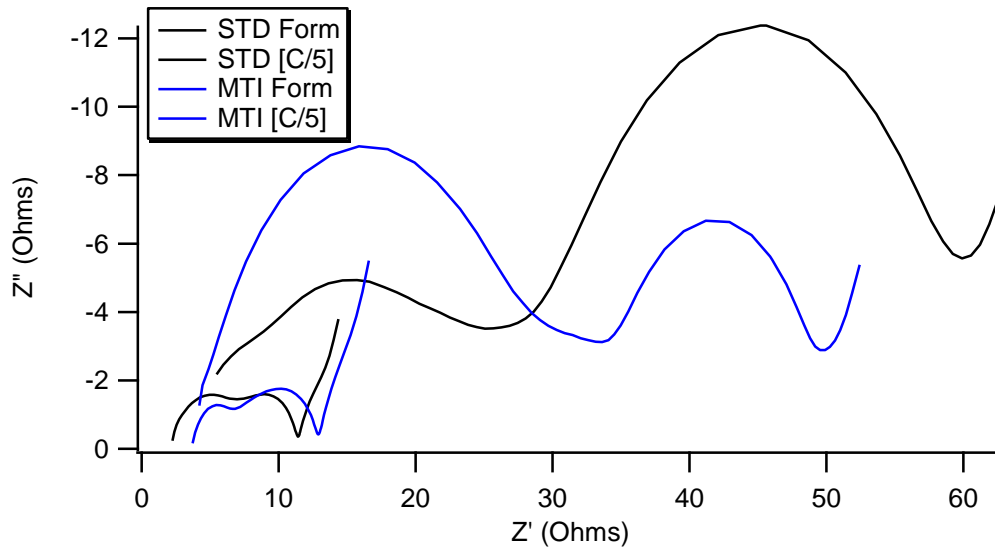


Figure 4.3: EIS of cells that cycled for 200 HT cycles at a [C/5] rate compared to cells that only cycled formation cycles.

Figure 4.4

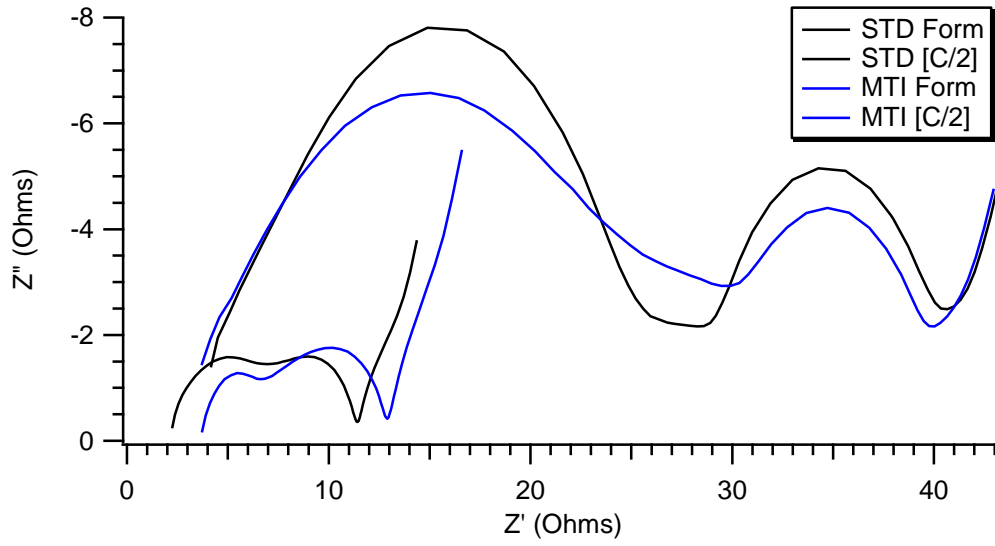


Figure 4.4: EIS of cells that cycled for 200 HT cycles at a [C/2] rate compared to cells that only cycled formation cycles.

Figure 4.5

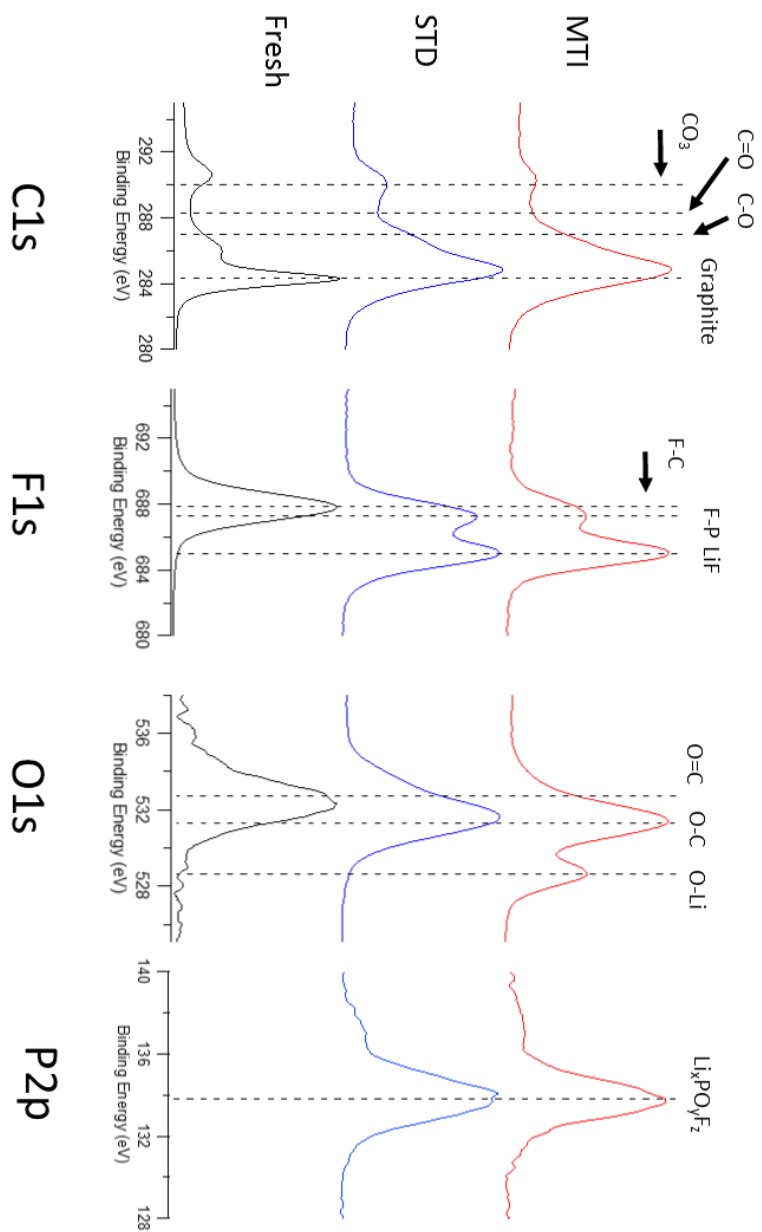


Figure 4.5: XPS of the anode for fresh, standard cells, and MTI cells.

Figure 4.6

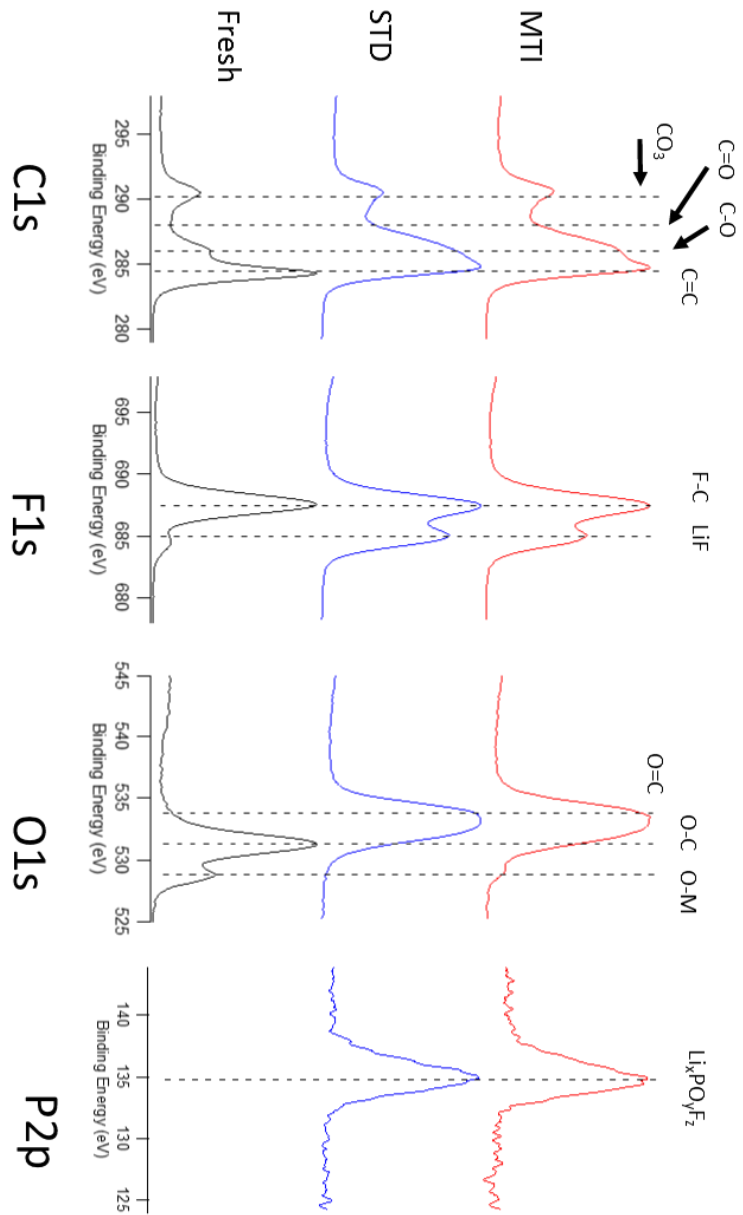


Figure 4.6: XPS of the cathode for fresh, standard cells, and MTI cells.

Figure 4.7

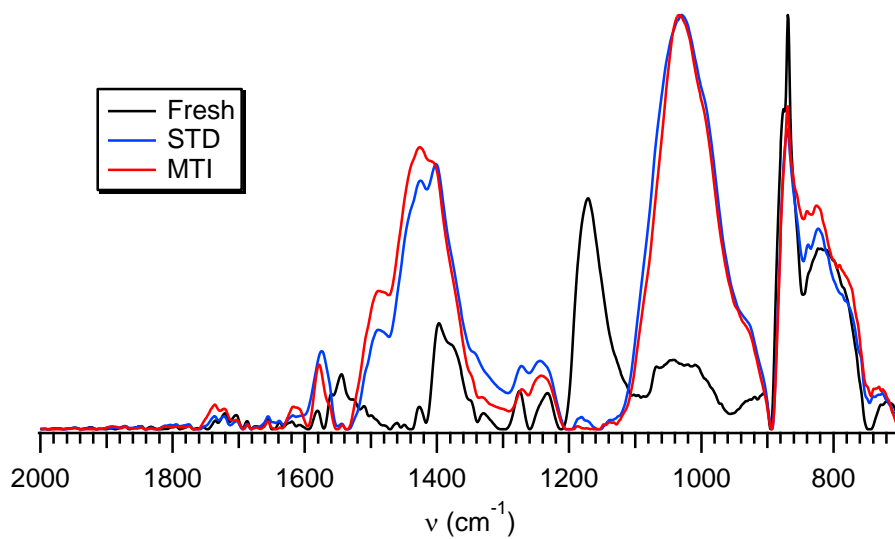


Figure 4.7: FTIR-ATR of anodes for fresh, standard cell and MTI cell.

Figure 4.8

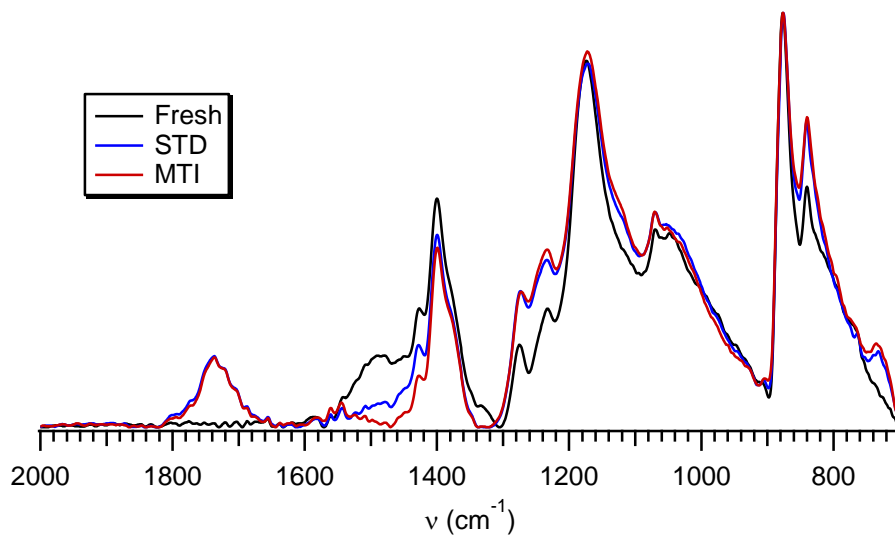


Figure 4.8: FTIR-ATR of cathode samples fresh, standard cell and MTI cell.

Table 4.1

	Fresh	STD	MTI
% [C]	42.5	21.7	42.8
% [O]	2.4	44.1	44.0
% [F]	55.1	31.5	10.2
% [P]	0.0	2.7	3.1

Table 4.1: Elemental concentration of anode samples derived from XPS.

Table 4.2

	Fresh	STD	MTI
% [C]	59.2	51.2	50.6
% [O]	9.6	18.5	17.7
% [F]	24.5	25.3	25.4
% [P]	0.0	1.9	1.8
% [Co]	<0.1	<0.1	<0.1
% [Al]	4.5	1.5	2.6
% [Ni]	2.1	1.7	1.9

Table 4.2: Elemental concentration of cathode samples derived from XPS.